ΠΑΝΕΠΙΣΤΗΜΙΟ ΠΑΤΡΩΝ
ΤΜΗΜΑ ΜΗΧΑΝΟΛΟΓΩΝ ΚΑΙ ΑΕΡΟΝΑΥΠΗΓΩΝ ΜΗΧΑΝΙΚΩΝ
ΑΕΡΟΝΑΥΠΗΓΟΣ
ΕΡΓΑΣΤΗΡΙΟ ΤΕΧΝΙΚΗΣ ΜΗΧΑΝΙΚΗΣ ΚΑΙ ΤΑΛΑΝΤΩΣΕΩΝ

Diploma Thesis

Design, Analysis and weight optimization of a UAV wing

Ioanna Vasilakopoulou Trapali

1054536

Supervisor: Vasileios Kostopoulos, Professor, Laboratory Director: Applied Mechanics Laboratory.

Patras, October 2022

Ioanna Vasilakopoulou Trapali

Design, analysis and weight optimization of a UAV wing.

Abstract

This thesis is a study for the design and optimization of a small wing, which will satisfy specific requirements for the mission of an unmanned aerial vehicle. In the design process, the determination of the initial individual values of the construction weight of the air vehicle was carried out by an iterative procedure and the accurate calculation of the wing loading and power loading, W/S and W/P respectively, parameters of the vehicle were estimated by a geometric method through a summary diagram to simultaneously satisfy all mission requirements. The initial estimates in the wing design were validated and redefined in the detailed design phase. This step formed the basis of aerodynamic analyses using the Finite Element Method (FEM) in ANSYS FLUENT software. The model with the initial approximation of the position and dimensions of the internal and external structures of the wing was designed in CATIA V5. At this point it was necessary to investigate methods of coupling the aerodynamic analyses and structural results through the interaction of the aerodynamic analysis solutions and its application on the wing surface (one-way Fluid Structure Interaction FSI analysis) to simulate the loads stressing the vehicle in flight and investigate its structural stability under real conditions rather than simplified non-continuous loading. In the experimental configuration of the wing, its structural response was studied with both aluminum alloys and composite materials. The application of composite materials was necessary to minimize the structure weight and a reduction of up to 50% was achieved. However further optimization of the structure led to the parameterization process of all wing parts and then the application of optimization algorithms through coupling them with the results of the FEM model. Optimal values for the position and thickness of the internal structures (ribs, spars, skin) were determined and a reduction of the structure weight from the initial wing configuration to the parametric design phase of up to 60% was achieved.

Key words: UAV wing, Conceptual Design, ANSYS FLUENT, CATIA V5, one-way FSI methods, optimization algorithms.

Ιωάννα Βασιλακοπούλου Τράπαλη

Σχεδιασμός ,ανάλυση και βελτιστοποίηση πτέρυγας μικρού μη επανδρωμένου αεροσκάφους για την ελαχιστοποίηση του βάρους κατασκευής.

Περίληψη

Η παρούσα εργασία αποτελεί αντικείμενο μελέτης για τον σχεδιασμό και την βελτιστοποίηση μικρών διαστάσεων πτέρυγας, η οποία θα ικανοποιεί συγκεκριμένες απαιτήσεις για την αποστολή μη επανδρωμένου εναέριου οχήματος. Στη διαδικασία σχεδιασμού, ο προσδιορισμός των αρχικών επιμέρους τιμών του βάρους κατασκευής του εναέριου οχήματος περατώθηκε με επαναληπτική διαδικασία και ο ακριβής υπολογισμός των παραμέτρων *W/S* και *W/P* του οχήματος εκτιμήθηκε με γεωμετρική μέθοδο μέσω συγκεντρωτικού διαγράμματος για την ταυτόχρονη ικανοποίηση όλων των απαιτήσεων της αποστολής. Οι αρχικές εκτιμήσεις στον σχεδιασμό της πτέρυγας επικυρώθηκαν και επαναπροσδιορίστηκαν στην φάση του λεπτομερούς σχεδιασμού .Το βήμα αυτό αποτέλεσε την βάση αεροδυναμικών αναλύσεων με την μέθοδο των πεπερασμένων στοιχείων στο λογισμικό ANSYS FLUENT. Το μοντέλο με την αρχική προσέγγισή της θέσης και των διαστάσεων των εσωτερικών και εξωτερικών δομών της πτέρυγας σχεδιάστηκε στο CATIA V5. Στο σημείο αυτό κρίθηκε απαραίτητη η έρευνα μεθόδων σύζευξης των αεροδυναμικών αναλύσεων και των δομικών αποτελεσμάτων μέσω της αλληλεπίδρασης των λύσεων των αεροδυναμικών αναλύσεων και την εφαρμογή του επάνω στην επιφάνεια της πτέρυγας για την προσομοίωση των φορτίων που καταπονούν το όχημα κατά την πτήση και την διερεύνηση της δομικής του ευστάθειας σε πραγματικές και όχι απλοποιημένες μη συνεχείς φορτίσεις. Στην πειραματική διαμόρφωση της πτέρυγας μελετήθηκε η δομική της απόκριση τόσο με κράματα αλουμινίου όσο και με σύνθετα υλικά. Η εφαρμογή σύνθετων υλικών ήταν απαραίτητη για την ελαχιστοποίηση του βάρους κατασκευής και επιτεύχθηκε μείωση έως και 50%. Ωστόσο περαιτέρω βελτιστοποίηση της κατασκευής οδήγησε στην διαδικασία παραμετροποίησης όλων των δομών της πτέρυγας και στη συνέχεια την εφαρμογή αλγορίθμων βελτιστοποίησης μέσω της σύζευξης τους με τα αποτελέσματα των μεθόδων πεπερασμένων στοιχείων. Προσδιορίστηκαν βέλτιστες τιμές για τη θέση και το πάχος των εσωτερικών δομών (ribs,spars,skin) και επιτεύχθηκε μείωση του βάρους κατασκευής από την αρχική διαμόρφωση της πτέρυγας στην φάση του παραμετρικού σχεδιασμού έως και 60%.

Λέξεις κλειδιά : πτέρυγα UAV, παραμετρικός σχεδιασμός, ANSYS FLUENT, CATIA V5, αλγόριθμοι βελτιστοποίησης.

Acknowledgments

I would like to thank my friends Nikos, Nota, Dimitra, and Kosmas for their love and support and my family who are always by my side in all my decisions.

I would also like to acknowledge my supervisor Vasilios Kostopoulos, whose collaboration give the chance to research and formulate this research design and Researcher Spiros Kilimtzidis and Eleftherios Nicholaou for their valuable support throughout this process.

Contents

List of Figures

List of Tables

Table of Symbols

W_{TO} : Take-off weight (kg)

W_E: Empty weight (kg)

W_{PL}: Payload weight (kg)

$W_{battery}$: Battery weight (kg)

E: Endurance (hrs)

n_{b2s} : Total efficiency

E_{sb}: Battery-specific energy (wh/kg)

Pused: Used power for a period (kW)

L: Lift force (N)

D: Drag force (N)

mb: battery mass (kg)

BMF: Battery mass fraction

V: UAV's velocity (km/h)

np: Propeller efficiency

W/P: Power loading (N/Watt)

W/S: Wing loading (N/m^2)

Preq: Required power (W)

C_L: lift coefficient

C_D: drag coefficient

C_{D0}: zero drag coefficient

q: dynamic pressure($kg/m\ s^2$)

Rt: battery hour rating

C: battery capacity (Ah)

i: discharge current (Amperes)

S: wing surface (m^2)

w: fluid velocity z-axis (m/s)

Vcruise: UAV's cruise speed

b: wingspan

AR: wing aspect ratio

e: Oswald coefficient

Λc/4: sweep angle ¼ chord (degree)

μ: dynamic viscosity (N · s / m)

Vs: stall speed (m/s)

Cr: root chord (m)

Ct: tip chord (m)

p_{sl}: density at sea level (kg/m^3)

σ: density ratio

R/C: rate of climb (m/s)

$P_{available}$: Available power (W)

E: aerodynamic ratio L/D

Re: Reynolds number

AoA: angle of attack (degree)

λ: wing taper ratio

M_x: bending moment (Nm)

S_y: shear force (N)

P_y: axial load (N)

q_s: shear flow

B: flange area (m^2)

dV: fluid control volume

u: fluid velocity x axis (m/s)

v: fluid velocity y-axis (m/s)

Fs: surface forces (N)

Fb: Body forces (N)

Fp: pressure forces (N)

Fv: viscous stress force (N)

τ: viscous stress tensor

eij: strain rate tensor

δij: Kronecker delta

e(T): total specific energy (W/kg)

Sg: Energy generation source(Watt)

y^+: *distance from the wall*

u^+:time-averaged velocity

τ_w: shear stress

Cf: skin friction coefficient

u_t: friction velocity

G_k: generation of turbulence kinetic energy

from velocity gradients

G_b: generation of turbulence kinetic energy

from buoyancy

σ_k, σ_ε : turbulence Prandtl numbers

μt: turbulence viscosity

a_o: airfoil lift slope

F_{wz}: force in panels (N)

K: stiffness matrix (Pa)

u: deformation vector (m)

E: Young Modulus (GPa)

G: Shear Modulus (GPa)

Fb: Body forces (N)

Fp: pressure forces (N)

1. Introduction

1.1 Motivation

The driving force of this work was my first flight in a Boeing 787. Being in a seat next to the wings of the airplane I kept observing the elastic deformation of the wings which are almost entirely manufactured with composite materials (carbon laminate). This fact particularly motivated my interest and so I wanted to deal with a topic that researches and analyzes the structural feasibility and behavior of wings with composite materials. The subject of this thesis is the development and design of a small-scale wing for an unmanned aerial vehicle. This subject was assigned to me as part of a project of the Applied Mechanics Laboratory for a full-scale analysis design and manufacturing of a small UAV.

Significant efforts invested in unmanned air vehicle technology led to a wide variety of new applications in the civilian community. Advances in avionics and electronics combined with rapid developments in the manufacturing processes of composite materials resulted in significant weight reduction, enhance efficiency, and quality improvements. A UAV can be equipped with simple electronic and physical sensors such as barometer, global positioning system receiver (GPS) and altimeter devices. Sophisticated UAVs can be equipped with photographic, infrared, acoustic equipment or even light detection and ranging laser along with radiation, chemical and other special sensors to measure specific parameters and accomplish critical missions. The on-board sensors can be controlled by ground-based operators or by automated remote operating mode .The capabilities of those systems present a serious alternative for missions such as surveillance of fishery activities, assessment of natural resources, and forest fire surveillance. The aim of this work is the development of a UAV design that can carry sensors and equipment for civilian use in specific payload weight range.

Figure 1. UAV for forest surveillance.

1.2 Research

This thesis suggests a practical way of designing and optimizing an electric-powered UAV. The experimental UAV meets certain mission requirements defined by the Laboratory project. The general idea is to end up with a fixed-wing UAV prototype with the necessary electronic and video equipment, depending on the mission that will perform. In the following sections an integrated analysis of the UAV conceptual and Preliminary design, aerodynamic analysis with CFD software, structural analysis of the experimental UAV wing, and structural optimization with available algorithms are presented. The analysis follows an iterative design process, in which the main purpose was the optimization of the design parameters in combination with the satisfaction of the mission requirements. Even at the Conceptual Design phase parameters such as velocity and battery power were defined in terms of Endurance and Range optimization to achieve maximum efficiency. The iterative process of the Conceptual design led to several trial designs which met the mission requirements, and further analysis and optimization were performed. Computational fluid dynamics analysis was performed in FLUENT software with the appropriate validation of finite elements model quality. The results were evaluated and validated by comparing them with results obtained by XFLR software and by analytical calculations. It was vital to predict, in the early phase of the design process, the structural behavior of the experimental wing. This could only be achieved by the deep understanding and simulation of the aerodynamic loads acting on the wing surface. Due to the high complexity nature of the phenomenon, several numerical techniques were developed to simulate the fluid-structure coupling and predict the structure performance as realistically as possible. Through the process of designing an efficient UAV, the need for more lightweight and competitive structures has given rise to the implementation of composite materials in the structures. A brief investigation of composite materials was performed to find the appropriate material and lamination method. Reaching some satisfactory designs at this point, considering the mass and performance requirements the next objective was a further optimized structure that cannot be obtained from manual simulations and intuition. This fact created the need for further investigation of structural optimization methods with the appropriate optimization tool, that coupled ant colony optimization algorithms with the Finite Elements model. The development and implementation of these advanced tools in structural optimization procedures led to minimum- mass structural designs. The fluid environment of the conceptual design. The importance of this thesis is that the fluid environment of the conceptual and preliminary design was deeply considered to develop various design models where the internal structures of the wing can be modified while the external characteristics are changing, reaching an optimum solution, that with the manual optimization would be infeasible.

2. Conceptual design

Conceptual design begins with the mission requirements of the aircraft. Design requirements have been presented in Table 1 and include Range, Endurance, payload, and speed requirements. The design begins even as a response to given requirements or as a development of a new innovative idea. Before an aircraft design begins an overview of the technology available to design a competitive product. The actual conceptual design begins with the estimation of the initial sizing that will provide data for an initial design layout and will operate as a basis of an iterative design process. The first estimation of the aircraft layout will end with a final concept that will be consistent with the mission requirements and other similar aircraft designs If the purpose of the study is not a revolutionary product. The next step is the Preliminary design. While further changes should be expected during preliminary design the initial shape of the aircraft will not change if the conceptual design is successful. The importance of this step is to ensure that CAD models that are developed will be tailored toward the fluid environment of the conceptual design. This can be interpreted in a fully parametrized model where the internal structures can be modified while the external characteristics are changing considering conceptual design and preliminary design.

The design process should be well organized. To better define the process, a system evolution model is described in Figure 2, where the process begins with the specification of a designing need. The design process can be considered to satisfy the following steps.

The *first step* is to precisely define the requirements of the designing model. This is a process of interaction between the designer and the sponsor. The *second step* of the design process is to develop a preliminary design of the system, where simplified models are used for several system concepts to be studied in a relatively short time. This is the first milestone in the design process since decisions at this stage can influence the system's final performance and form. A few models with satisfactory performance emerge at the end of this step, which should be further analyzed and evaluated. The *third step* is a detailed design for various subsystems, which are subject to an iterative process. To evaluate various possibilities, the design parameters of the system should be well defined. At this stage, an optimization process is started. The subsystems must be designed in a way that a performance measure of the system is optimized while several constrains and requirements are satisfied, and optimization methods aid the designer in accelerating the detailed design process. The important is that optimization concepts are helpful at every stage of this process, such methods with the appropriate software can lead to rapidly evaluating various subsystems and finding an optimum design, that with manual optimization would be Infeasible.

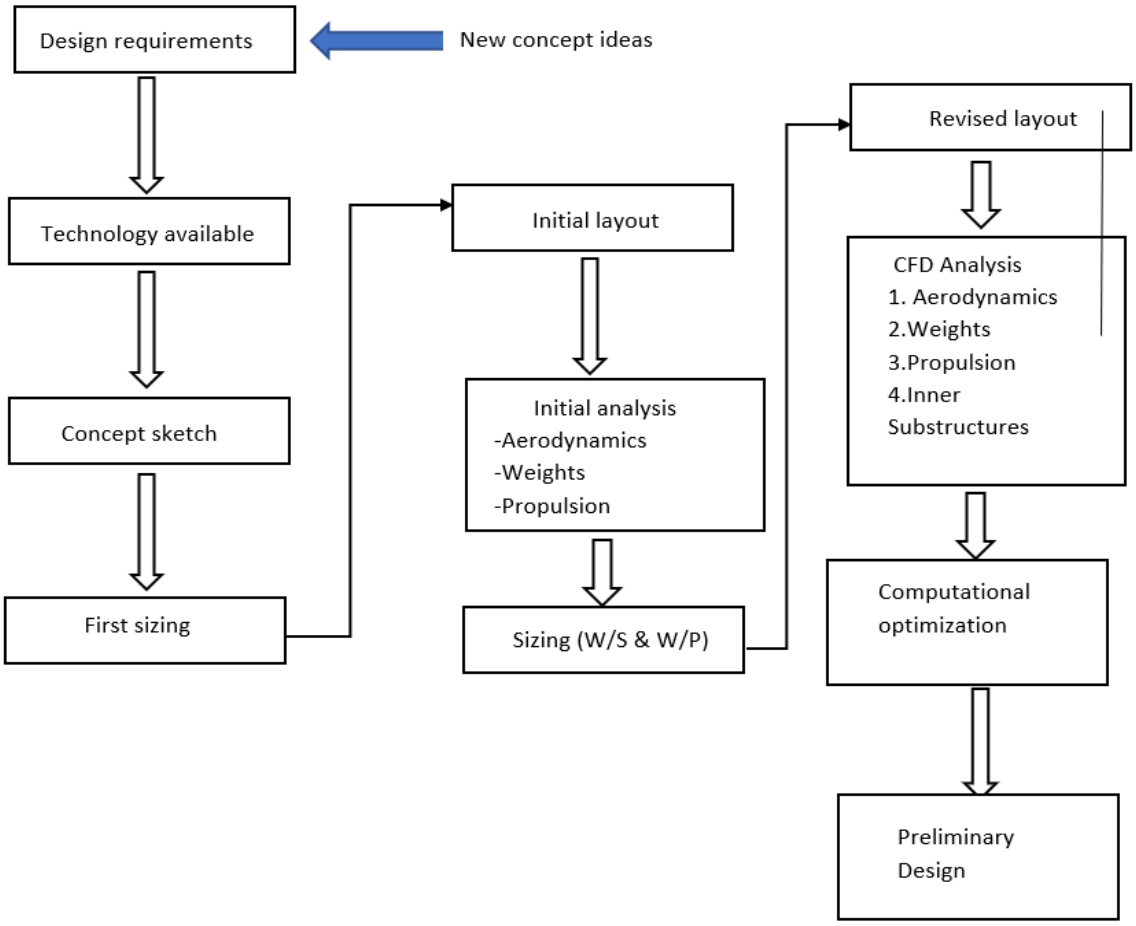

Figure 2. Conceptual Design roadmap

2.1 Mission Requirements

The design process starts with the mission requirements, presented in Table 1. This specification cannot be violated, and the final design should meet the mission constraints set for the mission objective. Due to the constraints, the experimental UAV is classified in the medium class and close Range.

Parameter	*Values*
Wingspan	<2.3m
Maximum W_{TO}	<11kg
Maximum takeoff ceiling	500m
Climb Rate	> 4 m/s
Cruising Altitude	200-500m
Maximum Operational Ceiling	1500 m
Cruise speed	≥22.2 m/s
Range	≥ 40 km
Max Endurance	≥ 35 min
Take-off	Catapult
Propulsion	Electric

Table 1. *Mission requirements.*

2.2 Take-off Weight Estimation for the Electric UAV

The first step of the conceptual design is the estimation of the total weight of the UAV which remains the same during the operation due to the electric propulsion. The total weight of an electric UAV can be divided into three parts: empty weight (W_E),battery weight ($W_{battery}$), *and* payload weight (W_{PL}) [1].

It can be assumed:

$$W_{to} = W_E + W_{PL} + W_{battery} \ (1)$$

W_{TO}	≈11kg
W_E	≈2.6kg
$W_{PAYLOAD}$	≈6.5kg

Table 2. *Initial weights layout*

Analysis for an Electric UAV starts with the estimation of the total flight Endurance as described below:

$$E = m_b * E_{sb} * \frac{n_{b2s}}{1000 * P_{used}} (2)$$

Where:

m_b is the mass of the batteries (kg)

E_{sb} is the battery-specific energy ($w * \frac{h}{kg}$)

n_{b2s} is the total efficiency of the system

P_{used} is the power used during a specific period (kW)

This Eqn. 2 is a simplified form to calculate the Endurance of an electric vehicle based only on the motor's current power setting without considering the flight condition, the vehicle weight, or the propeller losses. For a propeller aircraft in level flight can be assumed:

$$P_{used} * n_p = T * v = D * v = \frac{w}{\frac{L}{D}} * v \quad (3)$$

From Eqn. 2,3 the Level of flight Endurance or Loiter time is:

$$E = 3.6 * \frac{L}{D} * E_{sb} * \frac{n_{b2s} * n_p}{g * v} * \left(\frac{m_b}{m}\right) (hrs) \quad (4)$$

For battery electric vehicles the iterative method for estimating the take-off weight differs from the classic method for fuel-burning aircraft. This method uses the mission segment weight fraction ($\frac{W_i}{W_{i-1}}$) which is an indirect estimation of the fuel burn between each mission's starting and ending time. The most important equations that calculate the weight fractions at each mission segment are Breguet Range and Loiter equations. The ratios are used in an iterative process to find the aircraft's take-off gross weight. For a battery-electric vehicle, a similar method can be defined but the Breguet equation cannot be applied in this case study. There is no fuel burned and hence no change in the aircraft weight during flight. In the case of electric vehicles, the required battery mass for each mission segment is developed and used in the iterative process. The new parameter is called Battery Mass Fraction (BMF) and is defined as the ratio of battery mass to the aircraft's total weight. The BMF values calculated for various mission segments are used in the iterative method similar to the weight fractions.

Battery mass fraction can be defined from Eqn. 5 as:

$$BMF = \frac{mb}{m} = \frac{Wb}{W} = E * v * \frac{g}{3.6 * E_{sb} * n_p * n_{b2s} * \left(\frac{L}{D}\right)} \quad (5)$$

Where n_p is the propeller efficiency and v is the *UAV's velocity (km/h).*

The total required aircraft Battery mass fraction is then found as the sum of the various mission segment Battery Mass Fractions. The calculated BMF values for mission segments in terms of Wto can be expressed as:

$$W_{TO} = \frac{W_{payload}}{1 - BMF - \frac{W_E}{W_{TO}}} \quad (6)$$

This equation is the basic Electric Aircraft sizing equation.

The UAV mission can be divided into the different phases of flight, which are the following:

1. Take-off
2. Climb
3. Cruise
4. Descent
5. Loiter

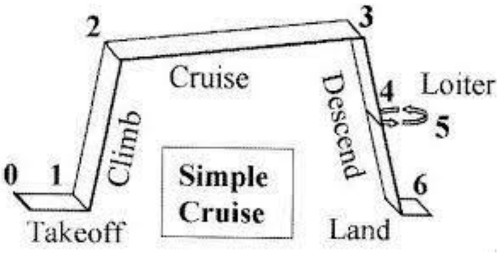

Figure 3. *Phases of UAV mission.*

The phases that are considered in the iterative method with the L/D and np values are shown in Table 3 below. The values are taken from historical data for electric vehicles.

	Cruise	*Loiter*
L/D	*11*	*12*
n_p	*0,7*	*0,6*

Table 3. *Values for L/D and propeller efficiency in different flight phases.*

The iteration method follows the above steps:

- Estimate Wto from UAV Tables
- Calculate W_E based on the logarithmic equation (Eqn. 7).

$$W_E = 10^{\left(-A+\frac{logW_{To}}{B}\right)} \quad (7)$$

Where the values of A, and B can be assumed from historical Tables for vehicles with composite materials as A=0.822 and B=0.805 [2].

- Estimate the parameter W_E/W_{TO}
- Calculate BMF for each mission segment
- Calculate W_{to} based on Eqn. 6
- Specify the divergence.

$$\varepsilon = \frac{|W_{TO1} - W_{TO2}|}{W_{TO1}} \quad (8)$$

- If $\varepsilon \leq 1\%$ the initial assumption was correct and $W_{TO} = W_{TO1}$
- If $\varepsilon \ngeq 1\%$ the iterative method continues.

After the iterative process is carried out in Matlab the values of the weights are obtained as follows. The estimated total weight of the electric UAV is 10.56 kg, the empty weight is 2.14kg, and battery weight is 1.92 kg, and the payload weight which was a mission requirement is 6.5 kg as given.

W_{TO}	10.56 kg
W_E	2.36 kg
$W_{PAYLOAD}$	6.5 kg
$W_{battery}$	≈1.7 kg

***Table 4**. Estimated final UAV weights*

The detailed calculation of the battery weight will be defined in the next paragraph as it depends on data that are not considered in this iterative method, and one should calculate them separately. The battery weight is derived based on the estimated range and endurance requirements.

2.3 Estimation for power loading

For homebuilt composite airplanes the power loading is estimated at first with analytical methods :

$$\frac{P}{W} = a * v_{max}^{c}$$

Where ***a=0.004, c=0.57*** [1]

A value for the first estimation of the power loading is $\frac{W}{P} = 0.25 \frac{N}{Watt}$.

2.4 Maximize Endurance and estimating Battery weight

In this chapter expressions that estimate the Range and Endurance of a battery-powered electric aircraft are described with the appropriate equations, accounting for the behavior of the battery and its effective capacity, depending on the current draw in the Peukert effect [3]. The main goal in the designing process is to optimize the efficiency of battery energy based on the battery energy density and the structural weight requirements. With the interaction between lift and drag forces, there is a specific cruise speed that minimizes the power requires for a specific cruise altitude. The optimal UAV design can reduce aircraft costs. The power required curve can further be used to find the velocity at which an airplane should fly to achieve maximum endurance. Endurance is maximized when the power required is minimized. Therefore, the velocity at which power required is a minimum is also the velocity for maximum endurance.

For an aircraft in steady flight the power required (Preq) is expressed as:

$$P_{req} = D \times U \ (9)$$

The drag polar for an aircraft is approximated

$$C_D = C_{D0} + \frac{C_L^2}{\pi * A * e} \qquad (10)$$

$$D = qS \left(C_{D0} + \frac{C_L^2}{\pi * A * e}\right) (11)$$

For parasitic drag C_{D0} :

$$C_{D0} = C_f * \frac{S_{wet}}{S} = 0.01 \ (12)$$

$$S_{wet} = 10^c * Wtotal^d \ \ (13)$$

Where **c=0.0199, d=0.4319, Cf=0.003.**

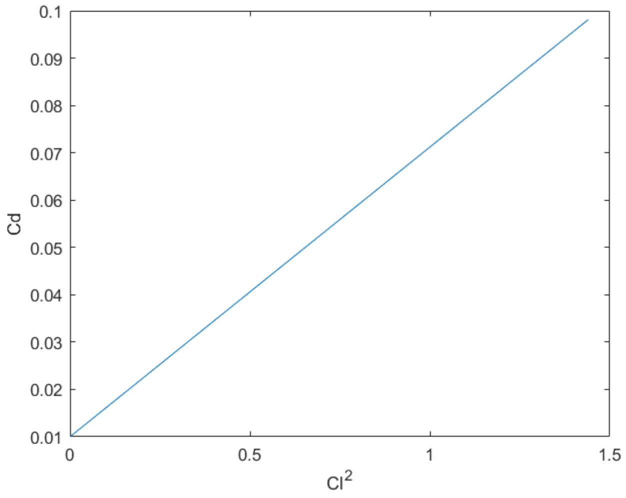

Figure 4. Drag polar

Assuming steady flight, where:

$$L = W = 0.5pV^2SC_L \ (14)$$

Based on Eqn. 12 and substituting into Eqn. 11 the power required for a steady flight is:

$$P_{req} = 0.5pV^3SC_{D0} + \frac{2W^2k}{pVS} \ (15)$$

Where $k = \frac{1}{\pi Ae}$ from Eqn. 11 and C_{D0} can be calculated from Figure 4. For an electric aircraft, the power required to overcome drag is provided by the battery. The capacity of the battery is measured in ampere-hours. Considering the Peukert effect the higher the current draw, the less the effective battery capacity. Peukert's law becomes a key issue in a battery electric vehicle, where batteries rated, for example, at a 20-hour discharge time are used at a much shorter discharge time of about 1 hour [4]. Peukert's equation can be expressed as:

$$t = \frac{Rt}{i^n}\left(\frac{C}{Rt}\right)^n \ (16)$$

Where Rt is the battery hour rating, C is the battery capacity in ampere-hours, i is the discharge current and n is a discharge parameter dependent on the battery type and temperature. For a battery the output power is:

$$P_B = V_i = V\frac{C}{Rt}\left(\frac{Rt}{t}\right)^{\frac{1}{n}} \text{ (17)}$$

The power output will be reduced due to the propulsion system losses. The losses are combined into a value named n_{total} .The result of Eqn. 15,17 is:

$$\frac{C}{Rt}\left(\frac{Rt}{t}\right)^{\frac{1}{n}} = \frac{1}{Vn_{total}}\left(0.5pV^3SC_{D0} + \frac{2W^2k}{pVS}\right) \text{ (18)}$$

In terms of flight time, Endurance is calculated as:

$$E = Rt^{1-n} * \left(n_{total}V\frac{C}{0.5pV^3SC_{D0} + 2W^2\frac{k}{pVS}}\right)^n (hrs) \text{ (19)}$$

From Eqn. 18 the endurance curve will be calculated concerning flight velocity and the values of parameters are specified in Table 5.

Rt	1h
n_{total}	0.5
S	0.81 m^2
W	103.44 N

Table 5*. Analytical values to estimate the Endurance curve*

Eqn. 18 can be used to estimate the endurance of the UAV concerning the discharge rate of the battery for any flight velocity.

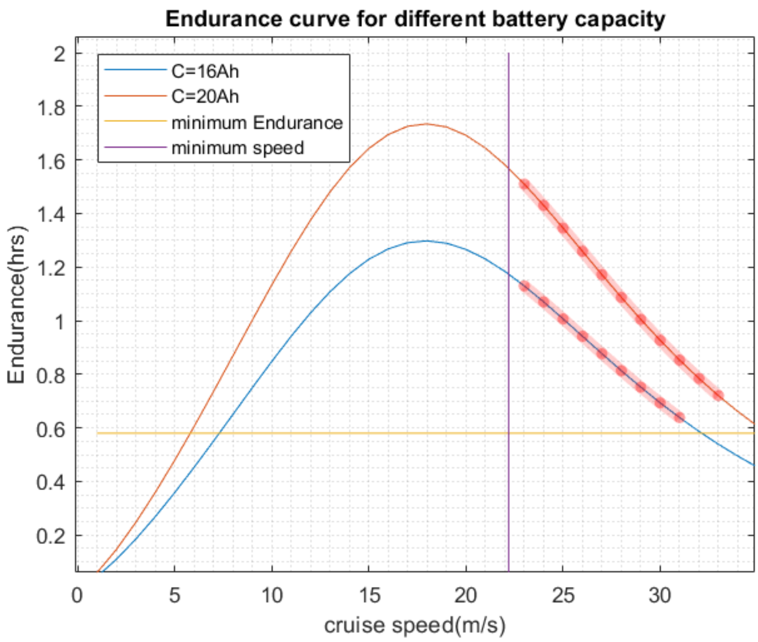

Figure 5. *Endurance curve for different battery capacities*

The Endurance has been tested for two different types of batteries.

Turnigy High Capacity 20000mAh 6S 12C Lipo Pack w/XT90	1.775 kg
Turnigy High Capacity 16000mAh 6S 12C Lipo Pack w/XT90	1.366 kg

Table 6. *Batteries for electric UAVs*

The results from Figure 5 are that the appropriate flight speed for the optimization of Endurance is close to the limit of mission requirement for flight speed and the battery pack that is used in the experimental UAV is Turnigy High Capacity 20,000mAh 6S 12C Lipo Pack w/XT90 with a mass of 1.775 kg which is inside the initial guess of battery mass.

The Endurance for a cruise speed of 22.5 m/s is 1.3886 hours or 83.316 minutes, which is compatible with the mission requirements.

For the Range:

$$R = E * v_{cruise} = 112{,}47 \text{ km} \quad (7)$$

Eqn.7 satisfy the mission requirement for a ***Range≥40 km.***

2.5 Selection of thrust and wing loading

2.5.1 Sizing to stall speed requirements

The stall speed of an aircraft is determined by the wing loading and the maximum lift coefficient. The wing loading concerning the stall speed requirement can be specified by the simple fact that lift equals weight at cruise conditions. Eqn. 20 combines stall speed with C_{Lmax}, noting that at the stall speed the aircraft is at maximum lift coefficient. By specifying a maximum stall speed that will not be around the region of cruise speed at operation altitude, Eqn. 20, defines the maximum wing loading for a constant C_{Lmax}.

$$\frac{W}{S} \leq \frac{1}{2} * p_0 * C_{Lmax} * v_{stall}^2 \quad (20)$$

From historic Tables [2] $C_{Lmax} = 1.2$ with a constant value.

Because there is no mission requirement for minimum stall speed the criterion will be applied for different stall speed values to achieve the maximum allowable wing loading.

2.5.2 Sizing to cruise speed requirements

This criterion requires that the aircraft speed must be equal to or greater than the normal airspeed. When the aircraft is flying at a specific cruise speed at a constant altitude :

$$\frac{T}{W} \geq C_{D0} * \frac{q}{\frac{W}{S}} + \frac{\frac{W}{S}}{pi * q * AR * e} (21)$$

Where the formula for estimating C_{D0} has been analyzed above. For the propeller-driven aircraft Eqn. 21 can be expressed as:

$$\frac{W}{P} \leq \frac{n_p}{C_{D0} * \frac{q}{\frac{W}{S}} + \frac{\frac{W}{S}}{pi * q * AR * e}} * v_{cruise} \quad (22)$$

2.5.3 Maximum speed at cruising altitude

The cruising speed is 1.15 times the maximum lift-to-drag ratio speed. The maximum speed is 1.2 times the cruising speed. The maximum lift-to-drag ratio speed is:

$$v_E = \sqrt{2/p(\frac{w}{s})\sqrt{\frac{K}{C_{D0}}}} \; (23)$$

The maximum engine output power (P_{max}) must be equal to the required power (P_{req}) at a constant velocity. Because required power decreases with the increasing flight altitude we have a dependence on air density. The power loading at sea level is :

$$n_{pr} P_{max} = v_{max} D \; (24)$$

$$\frac{P_{SL}}{Wtotal} n_{pr} \sigma = 0.5 p V^3 S C_{D0} + \frac{2W^2 k}{pVS} \; (25)$$

$$\frac{W}{P_{SL}} = \frac{n_{pr}}{0.5 * p * C_{D0} * (v_{max}^3) + \frac{2k}{p * \sigma * v_{max}} * \left(\frac{W}{S}\right)} \; (26)$$

Where σ is the ratio of cruising speed altitude density and sea-level density.

2.5.4 Rate of climb criterion

The vertical component of the velocity is by definition the rate of climb of an aircraft (Fig. 6).

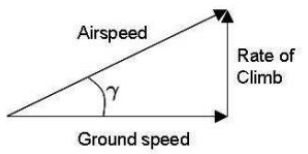

Figure 6. *Definition of climb rate about airspeed*

$$R/C = V_\infty sin\gamma \; (27)$$

$$\gamma = arcsin\left(\frac{R/C}{V}\right) \approx 10 \; deg \; (28)$$

The difference between the power available curve and the power required represents the excess power for a constant velocity climb. The rate of climb is the excess power divided by the airplane weight and is called R/C [1].

$$\frac{R}{C} = \frac{P_{available} - P_{required}}{W_{total}} \quad (29)$$

Thrust, drag, and the weight of the aircraft is the limitation for the climb performance of the aircraft. As the maximum RC value can be reached at sea level air density is used for the calculations.

$$V_v = n_p\left(\frac{P}{W}\right) - \frac{pV^3 C_{D0}}{2\frac{W}{S}} - \frac{2k}{pv}\left(\frac{W}{S}\right) \quad (30)$$

Taking in mind the estimation of thrust loading at the beginning of the chapter with the thrust matching method, Eqn. 30 can define the Rate of climb curve. The curve of the climb rate can be specified to see how the climb velocity (vertical velocity) changes for cruise speed. In the red area can see all the allowable value for R/C that satisfies the cruise speed criterion. It shows that the speed of 22.2 m/s is close to the region of the maximum rate of climb.

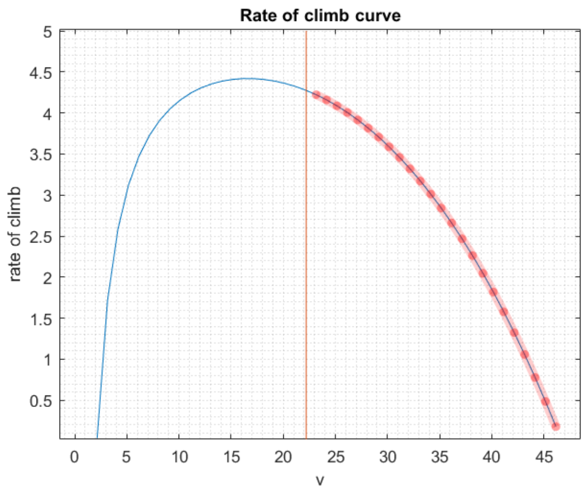

Figure 7. Rate of climb curve.

For a cruise speed v=23 m/s the climb (vertical velocity) is Vv=4.27 m/s. This value satisfies the mission requirement for a ***Rate of Climb ≥ 4m/s***

For this rate of the climb the criterion for defining the wing and thrust loading can be expressed as:

$$\frac{W}{P} = \frac{n_p}{\left(C_{D0} * \frac{q}{\frac{W}{S}} + \frac{\frac{W}{S}}{\pi * q * AR * e} + G\right) * vcruise} (31)$$

Where G=V_v/V.

The RC value is a denominator in the equations, so when the rate of climb is increasing, the value of power loading (W/P) is decreasing. Consequently, any value of RC greater than the one specified complies with the rate of climb requirements, and the region below the graph is acceptable.

2.5.5 Maximum ceiling

The maximum ceiling is the absolute ceiling the aircraft can safely have a straight flight. The absolute ceiling is the altitude at which the rate of climb is zero.

The matching plot can be created by using the same equation as for the calculation of climb rate. In the designing phase, the following approximation can be used for the relative densities

$$p_c = p_{sl}\left(\frac{p_c}{p_0}\right) = p_{sl}\sigma_{ac} (32)$$

$$\frac{W}{P} = \frac{\sigma}{\frac{RC}{n_p}\sqrt{(2 * (\frac{W}{S}))/p_c)}\sqrt{\frac{k}{3C_{D0}}} * \left(\frac{1.15}{E * n}\right)} (33)$$

For the maximum ceiling criterion RC=0 and Eqn. can be written as:

$$\frac{W}{P_{sl}} = \frac{\sigma_{ac}}{\sqrt{(2 * (\frac{W}{S}))/p_{ac})}\sqrt{\frac{k}{3C_{D0}}} * \left(\frac{1.15}{E * n}\right)} (34)$$

Where *E=L/D_{max}=11*. This value is obtained from similar aerial vehicles.

2.6 Matching all sizing Requirements

Having established a series of relations it is now possible to determine the best combination of these requirements for a first sizing estimation of the UAV. In this step, all requirements are considered, and the lowest possible power-to-weight ratio (maximum W/P) and the highest possible wing loading are selected which are consistent with all the sizing requirements. The preliminary design is completed using a geometrical approach with a matching plot that combines all the above requirements. The design problem is solved graphically, and the values of *wind loading,* and *power loading* can be specified. Figure 8 is shown a matching plot that is implemented in Matlab with all the above equations. The performance requirements are the cruise speed, the maximum speed, the stall speed, the climb rate, and the absolute ceiling. The maximum power loading (minimum power constrain) and the maximum wing loading can be satisfied at the intersection of the solid lines in Figure 8. The optimum design point is marked with the text arrow in the Matlab plot and the exact power loading and wing loading values are shown in Table 7.

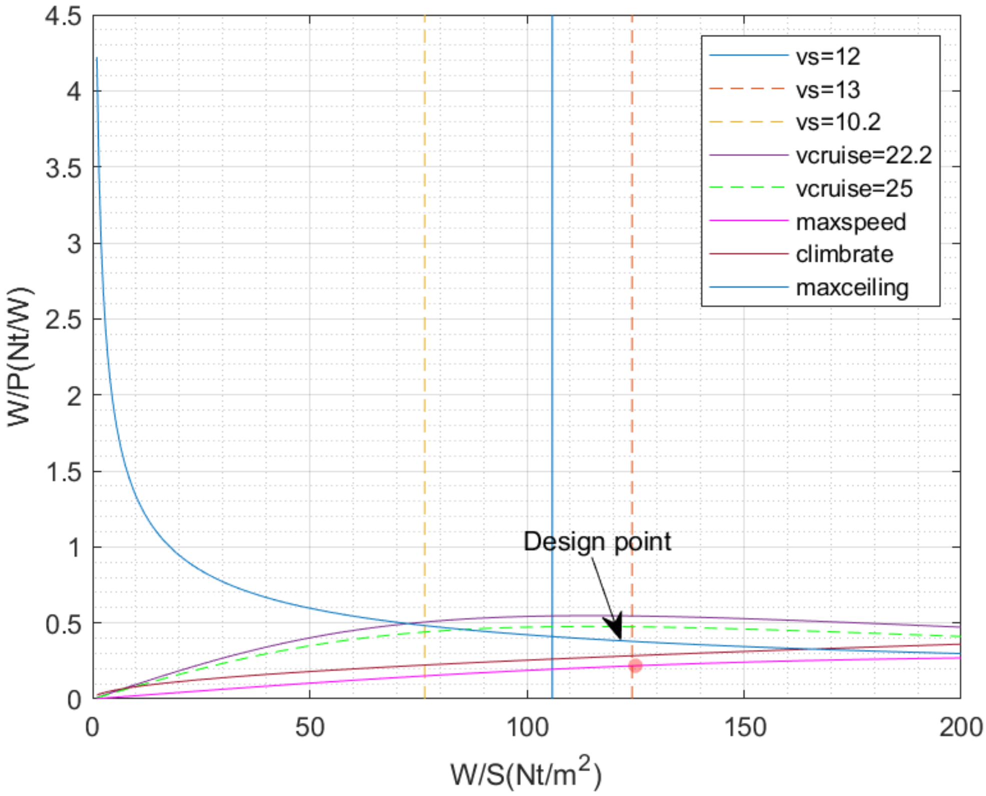

Figure 8. *The matching plot of the mission requirements of the experimental UAV*

W/P	***0.21 Nt/W***
W/S	***124.5 Nt/m^2***

Table 7. *Power loading and wing loading values.*

The sizing of the experimental UAV can be summarized with the following assumptions:

- The stall speed is specified as 13 m/s with a maximum lift coefficient of 1.2. The left area of the orange dashed line satisfies the criterion of stall speed.
- The maximum operating ceiling is 1500m as defined in the requirements. This is considered the absolute ceiling for the UAV mission and the climb rate is zero at this altitude. The criterion for the absolute ceiling is satisfied under the blue line in Figure 8. With the selected power loading the experimental UAV can operate safely up to this altitude.
- The optimum cruising speed is calculated by the optimization of the Endurance, Range, and Climb Rate criterion. Considering these parameters, the cruising speed has been specified close to the mission requirement limit. The UAV cruising speed is 22.5 m/s. For this speed, the power needs have been met in the area bellow the purple solid line.
- At cruising altitude, 500 m above sea level, the maximum speed is estimated as 1.2 times the cruising speed. The maximum speed has a value of 27 m/s. The power requirement for this criterion is satisfied in the area below the pink solid line.

The maximum power loading at the intersection of the purple line that satisfies the criterion of the cruise speed and between the area of the expected stall speed 10.2<vs<13 that satisfies all performance requirements simultaneously is 0.21 N/W and the associated wing loading is 124.5 N/m2. For these values, the surface of the wing based on the parametric design is 0.82 m^2. The estimated maximum energy consumption based on the power loading of 0.21 N/W is 490 W. A suggested model motor is AXI 4130/20 Gold line.

Figure 9. AXI 4130/20 motor for the experimental UAV

AXI 4139/20 specifications	
No of cells	***6-8s Li-Poly***
Max efficiency	***0.88***
Max efficiency current	***18-40 A***
Current capacity	***55A/60 sec***
Mass	***0.409 kg***
Min Power	$\mathbf{4.2 * 6 * 18 = 453\ W}$
Max Power	$\mathbf{4.2 * 6 * 40 = 1008\ W}$

Table 8. *The specification of the AXI 4139/20 MOTOR*

As it is shown in Table 8 the power requirements can be satisfied by the AXI 4139/20 motor. For reasons of clarity, the Matlab code used in this Chapter is presented in Appendix A.

3. Aircraft Aerodynamic design

3.1 Reynolds number

Reynolds number is the criterion used to determine whether the flow is laminar at turbulent. For flow over a wing, the transition from laminar to turbulent boundary layer occurs where Reynolds exceeds $Re_{x,crit} \approx 500{,}000$.For the flow over the wing root:

$$Re_l = \frac{pUc}{\mu} = 7.379 * 10^5 \ (35)$$

ρ: density $\xrightarrow{yields}$ p=1.1685 kg/m^3

u: the velocity of the fluid concerning the object

c: characteristic linear dimension (length of the chord)

μ: dynamic viscosity of the fluid $\xrightarrow{yields}$ μ=1.7735*10^{-5} at 500 m above sea level

Low Reynolds number airfoils

Low Reynolds number flows are often determined by the state of the boundary layer and the behavior of the boundary layer separation. For Re<5×10^4 the boundary layer is stratified and resistant to perturbations that can lead to the transition to a turbulent layer. The higher-pressure flow at the wing surface meets the free flow at the divergence rim, thus creating a region of strong pressure changes. For airfoils with Re> 10^6 the flow is within the turbulent boundary layer region and no detachment is easily observed. However, the strong pressure transitions encountered by the laminar boundary layer in regions with low Re numbers easily cause it to separate without a subsequent transition to turbulent flow and thus no reattachment of the boundary layer occurs. Consequently, this flow condition is characterized by low buoyancy coefficients and high drag coefficients. Hence, the performance of the airfoil in this type of flow is quite low [5].

When the Re number increases it becomes possible to transition the detached layer to turbulent flow. In this value range when the boundary layer is detached a rapid transition to turbulent flow and reattachment of the flow as a turbulent boundary layer can occur. This phenomenon is shown in Figure 11 and is called a "laminar separation bubble". These bubbles affect the aerodynamics of the airfoil, creating a non-linear lift distribution due to their displacement and increasing drag.

3.2 XFLR analysis

For UAVs, the airfoil is one of the most important components of their performance that will determine their success. A reasonable selection of wing airfoil is the most important part of the design process. The selected airfoil predetermines lift-to-drag ratio, altitude airspeed performance, stalling region, and Endurance as well. These reasons demand to investigate of the problem of UAV wing airfoil selection and considering the Reynolds number region that it operates.

To design a UAV, in general, the designer first has to gather all the requirements. After doing the initial sizing to have the operating Reynolds number and gathering the sizing baseline, the designer has to move to the configuration design where airfoil and aircraft configuration must be chosen then does many stages of the multidisciplinary analysis and the optimization to give out the optimum configuration.

The first airfoils were developed by Horatio F. Phillips in 1884 who made the first experiments with airfoils in wind tunnels. Then the pioneers were the Wright brothers who made the first flight in December 1903 after testing airfoils in a wind tunnel. Then, in 1930, the main pioneers who created airfoil shapes that are still used today were NACA, the predecessors of today's NASA [6].

The geometry of the airfoil is shown in Figure 10. In detail, the main geometric characteristics of an airfoil are as follows:

- The Airfoil Mean Line or Mean Camber Line is the geometric locus of the points equidistant from the top and bottom surfaces of the airfoil.
- The Leading Edge of the airfoil is the leading edge of the Mean Camber Line.
- The leading edge or Trailing Edge of the airfoil is the trailing edge of the center line.
- The Airfoil Chord or Chord Line is the straight line connecting the leading edge to the trailing edge.
- The Maximum Curvature of the Airfoil or Camber is the maximum distance between the Chord Line and the Centerline.
- Airfoil Thickness or Thickness is the distance between the top and bottom airfoil surfaces measured perpendicular to the string.

The shape of the airfoil is usually circular at the leading edge with an edge radius of 0.02c. Initially, all airfoils developed, especially NACA airfoils, are produced by determining the mean line of curvature and then by determining a symmetrical thickness distribution around the mean line.

The first family of NACA airfoils developed was the 4-digit NACA airfoils (4-digit NACA airfoils) such as NACA 4415 which will be the subject of the thesis.

Figure 10 shows the NACA 2415 airfoil as produced by Airfoil Tools [7].

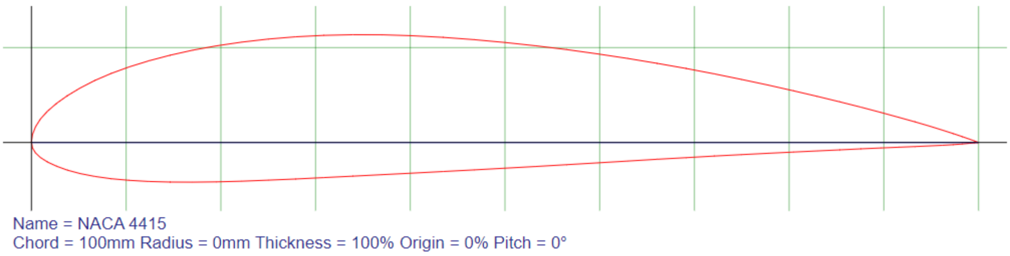

Figure 10. *NACA 4415 in airfoil plotter*

For the analysis of the airfoils, XFLR 5 is used. XFLR 5 is a tool based on XFOIL and JAVA FOIL software. This software uses the panel method to give a solution for vorticity and source distribution and other parameters such as lift drag and pitching moment can be determined. A list of airfoils is testified, and their performance is then evaluated.

NACA 0015 and NACA 4415 will at first be checked as they are the most common 4-digit and broadly used due to their aerodynamic shape. The NACA 0015 airfoil is symmetrical with no camber. The digit 15 demonstrates that the airfoil has a 15% thickness to chord length proportion, it is 15% as thick as it is long. The NACA airfoil 4415 has a greater camber of 4% located 40% (0.4 of the chord) from the main edge with a maximum thickness of 15% of the chord. Both NACA 0015 and NACA 4415 airfoil is examined to comprehend the transient progression of flow separation, lift, drag, pressure, and velocity contour.

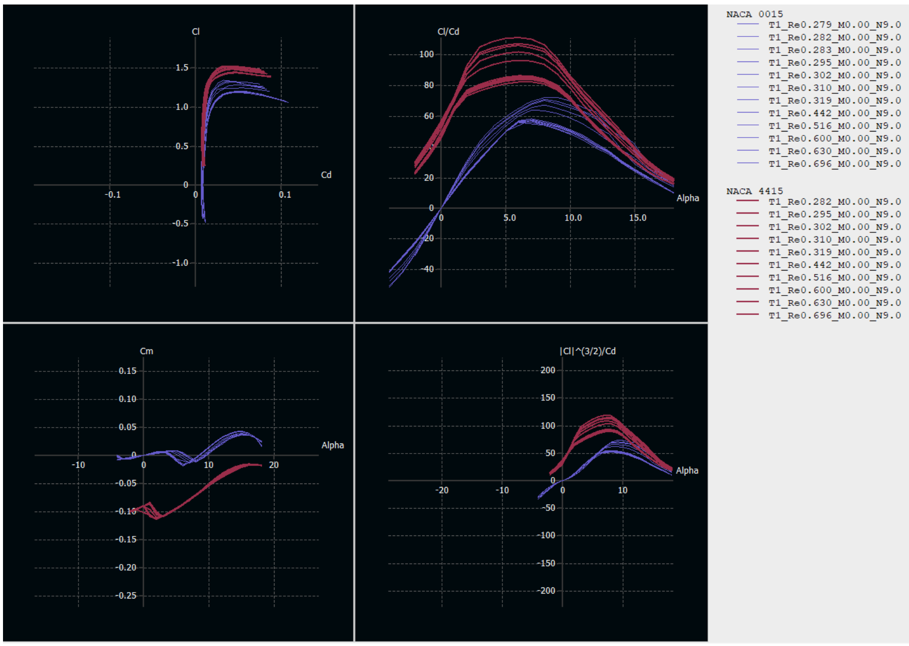

Figure 11. XFLR diagrams for two different airfoils

The analysis starts with Direct Foil Design and then after specifying an adequate number of points in the airfoils the next step is the Direct Foil Analysis. The Batch Analysis that is conducted has a range of 200.000<Re<700.000 for both airfoils. From the above analysis airfoil, NACA 4415 is preferred for its aerodynamic characteristics.

The main goal is to specify whether the initial values for Cl and Cd that was analytically calculated at the first step of the Conceptual design are satisfied. If they are not the iteration method and the application of the criterion that was presented above should be repeated.

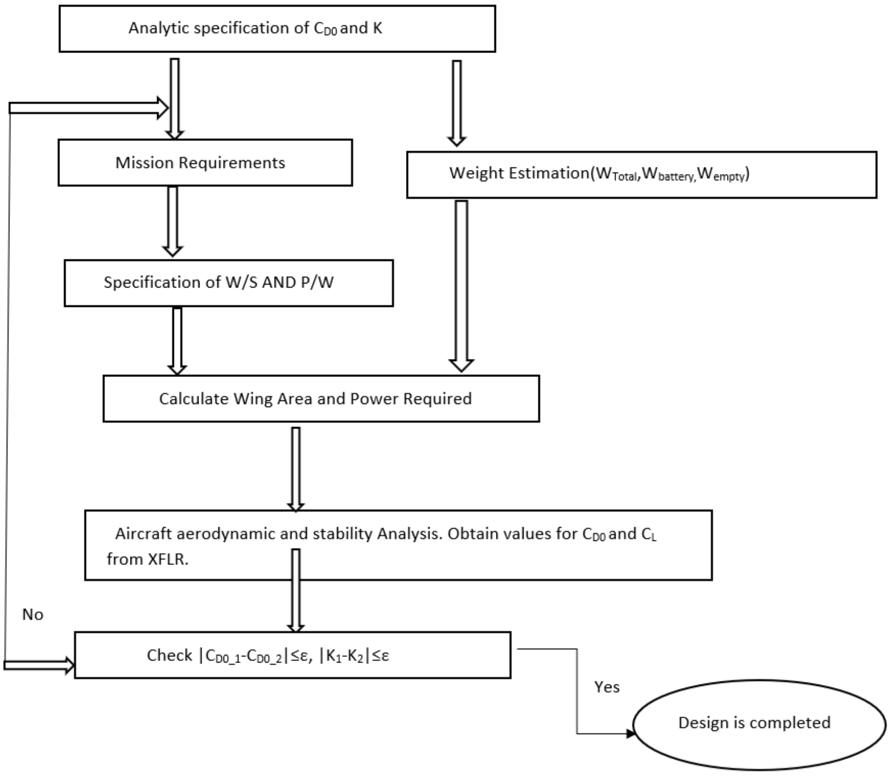

Figure 12. Evaluation of preliminary design

The calculated C_{d0} in Chapter 3 has been found C_{d0}=0.01. From XFLR it is obtained a value of C_{d0}=0.009. The iteration method presented in Chapter 4 may be carried out again with the new values from XFLR. The difference between the theoretical and the experimental result is quite small so the design process will be continued without the repetition of the parametric design.

3.3 Wing geometric parameters

The aerodynamic design of a wing mainly involves determining a wing planform that can maximize the lift and minimize the drag. The main platform parameters are the aspect ratio, sweep angle, and taper ratio. The aspect ratio affects the induced drag coefficient, zero-lift drag coefficient, and slope of the lift coefficient. An increase in the aspect ratio can reduce the wing's induced drag. A decrease in the aspect ratio prevents the wing tip stall under a high angle of attack and reduces the wing structure's weight and the bending moment at the wing root.

Considering the phase of conceptual design and the aerodynamic analysis the wing characteristics are shown below:

Wing Characteristics		
Zero lift drag coefficient	C_{D0}	0.009
Induced drag factor	C_{Di}	0.0507
Cruising speed	V_{cruise}	23 m/s
Maximum speed	V_{max}	27 m/s
Wing Area	S	0.81
Wing aspect ratio	AR	6.53
Wing angle of attack	AoA	3 deg

***Table 9**. Wing characteristics*

Wingspan	Root chord	Tip *chord*	Cruising Mach Number	Flight height
2.3	0.448	0.256	0.08	500 m

***Table 10.** Wing design parameters*

At an angle of attack of ***AoA=3***◦, the pitching moment coefficient is ***Cm=0.064*** and lift coefficient is ***Cl=0.5674*** and the zero-lift drag coefficient is ***Cd_0=0.01***

4. Conceptual structural design

After the preliminary design, a model in CATIA V5 was developed, and structural members are shaped. The design is a detailed design of both the external skin of the wing and the internal structure with the appropriate number of ribs and spars. The location of ribs and spars in this phase of the design will be determined by historical data tables from similar aerial vehicles. Later in the design process, their location and exact dimensions will be determined by the structural analysis and weight optimization process that will be discussed in the following chapters.

First, the coordinates of the airfoil NACA 4415 are imported into CATIA V5, as illustrated in Figure 13. Based on the theory of Flow over finite wings [6] the experimental wing is shaped with a taper ratio λ=0.57, Figure 14 and without a sweep angle as it is not preferred for low Reynolds number flows.

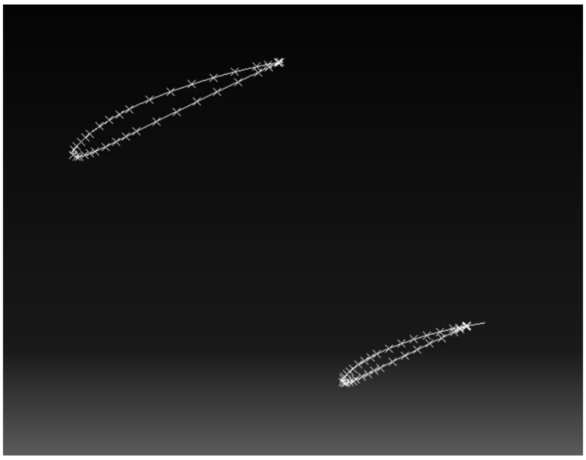

Figure 13. *Imported airfoil coordinates for NACA 4415airfoil*

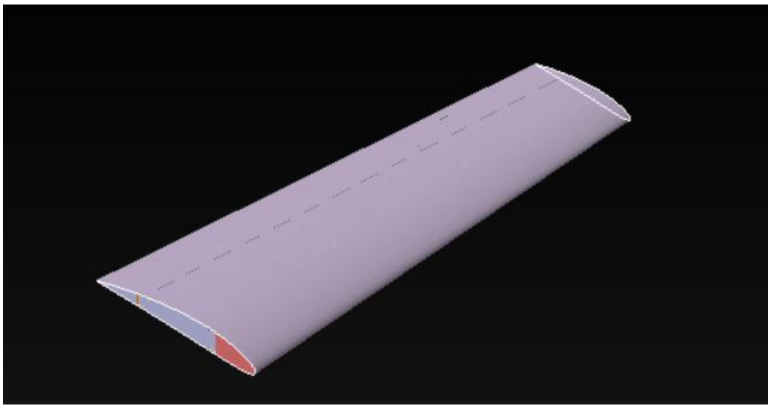

Figure 14. *Preliminary design of the experimental wing*

4.1 Internal structure

This phase of the design includes the selection of the shape of each structural part to achieve structural integrity and adequate strength. As the aerodynamic loads from aircraft wings are received by more than one structural element, the detailed analysis is very complicated, and the problem is simplified as a beam-bending moment problem.

4.1.1 Type of spars

Spars are the main load-bearing members in the wing. They are strong beams that run spanwise in the wing and carry the force and moments. Spars can have a rectangular cross-section; however, C-type or I-shaped cross-section areas are preferred as they have higher moments of inertia because they have their area further from the neutral axes where the stresses are maximum. A typical C-type spar is illustrated in Figure 15. The top and bottom portions of the spar are called spar caps and the thin piece of material connecting them is called spar web. The main structural load that the spar caps are subjected to are tension and compression while spar webs are designed to resist shear stresses[8].

Because the spar must fit within the wing, the shape and size chosen for the wing's airfoil determine the maximum possible height of the spar as shown in Figure 16. Spar webs can be quite thin as they primarily resist shear stresses that are relatively small compared to the stresses that are applied to the spar caps. Because they must primarily carry shear stresses, webs made of composite materials should have their fibers in a mesh or with multiple layers in which each layer has fibers oriented 90 deg or 45 deg relative to fibers in adjacent layers.

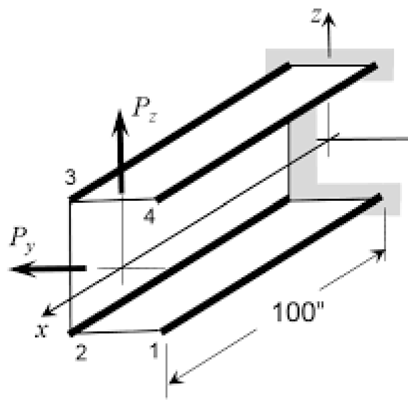

***Figure 15**. C-type spar*

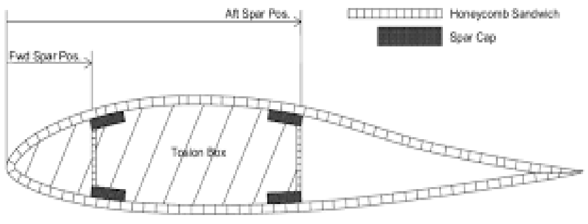

***Figure 16.** Spars with respect to the airfoil shape.*

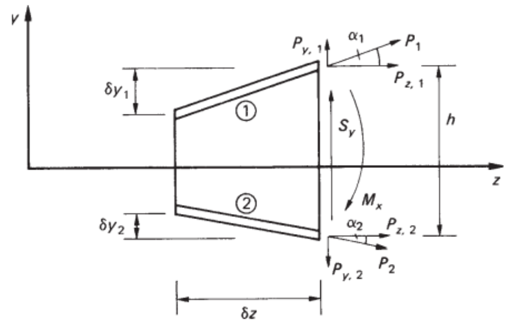

Figure 17. Tapered c-type spar with shear forces and bending moments.

Selected spars

The selected spar geometry is tapered along the length of the wing. Thus, the wing section is reduced both chordwise and in depth along the wingspan towards the tip. The selected spar has a C-type cross-section, and the analytic solution of the dominated shear stresses is demonstrated below.

An elemental length δz of the tapered beam is shown in Figure 17. At the z direction, the beam is subjected to a positive moment Mx and a positive shear force Sy. The bending moments are parallel to the z-axis and are calculated as:

$$P_{z1} = \frac{M_x}{h} = -P_{z2} \ (36)$$

The component of the axial loads parallel to the y-axis:

$$P_{y1} = \frac{P_{z1}\delta_{y1}}{\delta_z} \ (37)$$

$$P_{y2} = -\frac{P_{z2}\delta_{y2}}{\delta_z} \ (38)$$

The net axial load in the flange:

$$P_1 = \left(P_{y1}^2 + P_{z1}^2\right)^{\frac{1}{2}} \ (39)$$

The internal shear force includes the web shear flows $S_{y,w}$ and the vertical components P_1, P_2.

$$S_y = S_{y,w} + P_{y,1} - P_{y,2} \ (40)$$

Or

$$S_{y,w} = S_y - \frac{P_{z1}\delta_{y1}}{\delta_z} - P_{y2} - \frac{P_{z2}\delta_{y2}}{\delta_z} \ (41)$$

Eqn. 41 is an expression of shear stress flow in the web of the spar.

For a spar in which the web is fully effective in resisting direct tresses the shear flow distribution is:

$$q_s = -S_{y,w}/I_{xx}\int_0^s t_D y ds + B_1 y_1 \; (42)$$

Or

$$q_s = -S_{y,w}/I_{xx}\int_0^s t_D y ds + B_2 y_2 \; (43)$$

Where B_1 and B_2 are the flanges areas.

Location of spars

The two-spar wing construction usually consists of a front and rear spar, Figure 18. The front spar is located where the wing leading edge slats can be attached to it and the rear spar is located such as control surfaces such as flaps, ailerons, and spoilers can be attached to it. Front and rear spar combined with wing skin panels are the main members of the wing torsion resistance. The experimental wing model is parametrized in CATIA V 5 about the spar position. It is constructed with four possible positions for the front and rear spar. Table 11 is shown the internal position of ribs and spars about the chord of the root chord.

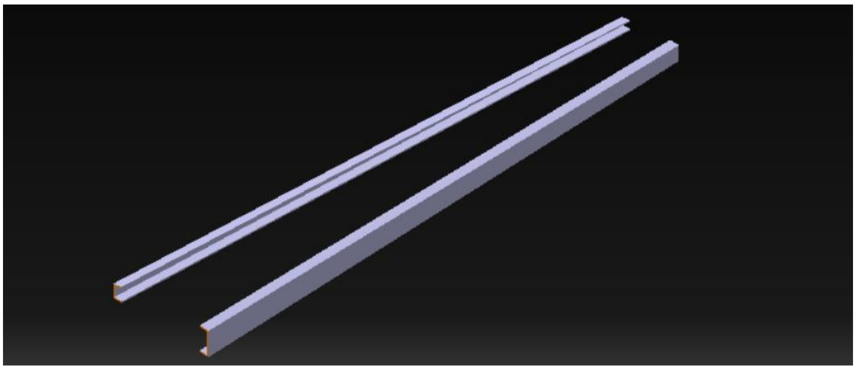

Figure 18*. Front and rear spar*

4.1.2 Ribs

The wing ribs extend from the leading edge to the trailing edge of the wing. The wing ribs can be divided into three areas, namely the leading and trailing edges rib portions and the wing box rib portion. The front and rear spars intervene between these three sections, where the rib is riveted into the webs. The main functions of the ribs are to maintain the shape of the wing cross-section for all combinations of load by increasing its rigidity. They maintain the shape, and they are transmitting external loads to the wing skin[9]. External loads applied in the plane of the rib produce a change in shear force in the wing across the rib.

Wing's ribs are mainly subjected to three kinds of loads.

- Aerodynamic loads from the skin included lift, drag force, and pitching moment.
- Gravitational forces and inertia forces concerning the wing structure mass.
- Concentrated transmitted forces from the landing gear, fuselage connections, and controlling surface structure connections[10].

The three components have been described with the basic structural shape to demonstrate the connection with spars, but the detailed way of the connection is out of the scope of this thesis.

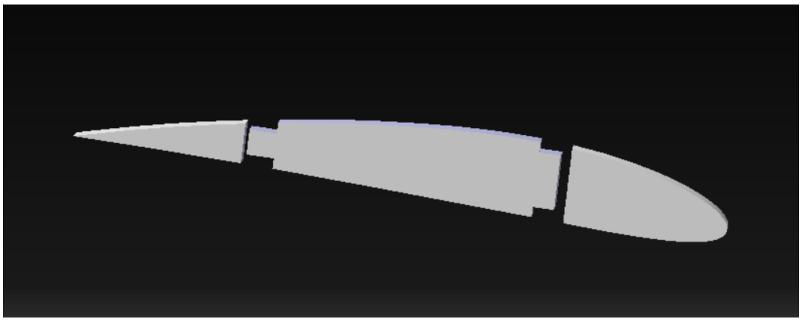

Figure 19. *Middle, trailing edge, leading edge rib*

4.1.3 Skin

The primary function of the skin of the wing is to form a surface for the development of the aerodynamic pressure distribution. These aerodynamic forces are in turn transmitted to the ribs and spars.

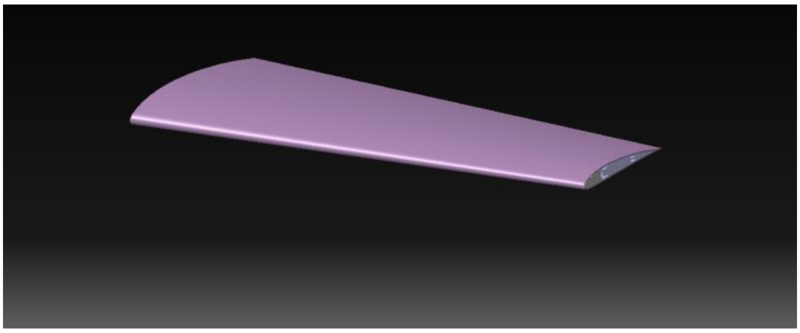

Figure 20. *Skin surface.*

4.1.4 Experimental Wing structure

The above analysis results in the configuration of the wing's internal structure as follows:

Components	*Position*	*Thickness*	*Chord* Length	*Length*
Rib (1)	Root	10 mm	448 mm	-
Rib (10)	Tip	10 mm	256 mm	-
Ribs (2 3 4 5 6 7 8)		4mm	424 mm 400 mm 376 mm 352 mm 328 mm 304 mm 280 mm	-
Front spar	10,%,25%,30%,35%(of root chord)	3 mm	-	1150mm
Rear spar	65%,70%,75%,80% of root chord)	3mm	-	1150mm
Skin	-	2mm	-	-

Table 11. *Geometrical properties of the wing*

The wing configuration is illustrated bellow. Figures 21,22,23 are shown the wing's internal structure, while the front and rear spar change position concerning the chord length.

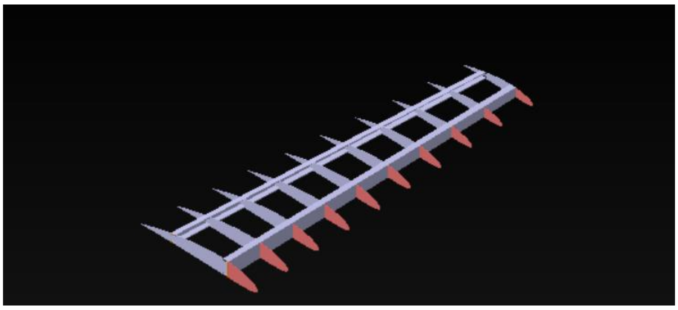

Figure 21. *Spars at locations 30%,75% respectively.*

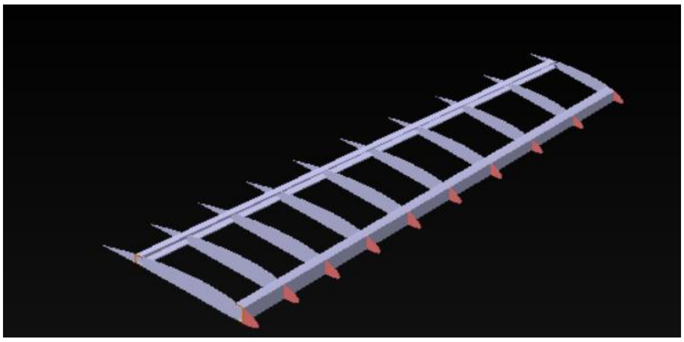

Figure 22. Spars at location 10%,80% respectively.

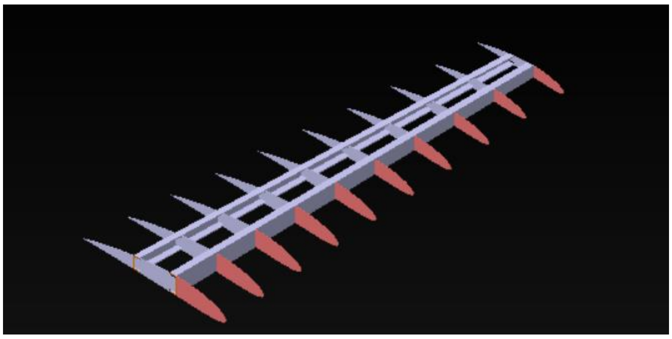

Figure 23. Spars at locations 35%, 65% respectively.

5. CFD analysis and Results

5.1 Numerical analysis and governing equations

Computational fluid dynamics obeys the fundamental governing equation of fluid dynamics. These equations are the continuity, momentum, and energy equations and they summarized in the above statements

- Conservation of mass.
- Newton's second law.
- Conservation of energy.

The above statements should be expressed as mathematical models to better investigate the governing equations of computational fluid dynamics[11].

5.1.1 The Continuity Equation

Physical principle: The mass can be neither created nor destroyed. Applied to a control volume the above physical principle means:

Net mass flows out of the control volume through the surface S ≡ time rate of decrease of mass inside control volume V.

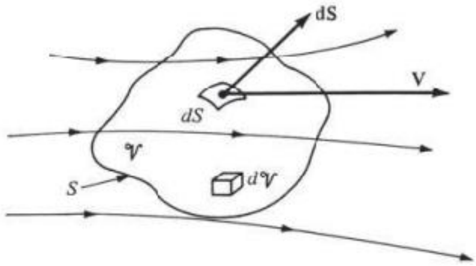

Figure 24. Fluid arbitrary volume.

Consider a fluid flow wherein all properties vary with spatial location and time. The Euler form of the conservation of mass is derived as follows :

Apply Reynolds Transport Theorem (*f=1*) [12]:

$$\frac{\partial}{\partial t}\oiiint p\ d\boldsymbol{\Omega} + \oiint p\ \boldsymbol{V}\ dS = 0\ (44)$$

Eqn. 44 is called the *Continuity Equation* and it is one of the most fundamental equations of fluid dynamics.

Apply the Divergence Theorem:

$$\oiiint \left(\frac{\partial p}{\partial t} + \nabla(p\boldsymbol{V})\right) d\boldsymbol{\Omega} = 0\ \ (45)$$

The finite control volume is arbitrarily drawn in space, there is no reason to expect the cancellation of one region by the other. Hence, the only way for the integral in Eqn. 45 to be zero for an arbitrary control volume is for the integrand to be zero at all points within the control volume.

The continuity equation in the form of a partial differential equation is:

$$\frac{\partial p}{\partial t} + \nabla(p\boldsymbol{V}) = 0\ \ (46)$$

It is convenient to express the above equation in a Cartesian form:

$$\frac{\partial p}{\partial t} + \frac{\partial(pu)}{\partial x} + \frac{\partial(pv)}{\partial y} + \frac{\partial(pw)}{\partial z} = 0\ (47)$$

5.1.2 Momentum equation

The physical principle of the Momentum Equation is the expression of Newton's second law. Applying the Reynolds Transport and Divergence Theorems to the conservation of momentum for the Lagrangian form (2nd Newton's Law) :

$$\frac{\partial}{\partial t}\oiiint p\boldsymbol{V}d\Omega + \oiint \boldsymbol{V}(p\boldsymbol{V}dA) = \boldsymbol{F_s} + \boldsymbol{F_b} \ (48)$$

Applying the divergence theorem and using the continuity equation the Eqn. 48 can be written as:

$$\oiiint (\frac{\partial(pu)}{\partial t} + \nabla(puU)) = \boldsymbol{F_s} + \boldsymbol{F_b} \ (49)$$

Surface forces acting on the fluid particle are due to pressure and viscous stress. The net pressure and viscous stresses can be expressed as:

$$\boldsymbol{F_S} = \boldsymbol{F_p} + \boldsymbol{F_v} \ (50)$$

Where:

$$\boldsymbol{F_p} = -\oiint p\,\boldsymbol{n}\,dA \ \ pressure\,force \ (51)$$

$$\boldsymbol{F_v} = \oiint \bar{\bar{\tau}}\,\boldsymbol{n}\,dA \ \ viscous\,stress\,force \ (52)$$

Where $\bar{\bar{\tau}}$ is the viscous stress tensor. Pressure acts normal to the surface whereas viscous stress has components that act both normal and tangent to the surface.

The pressure and viscous force can be transformed from a surface integral into a volume integral with the Divergence Theorem :

$$\oiint p\,\boldsymbol{n}\,dA = \iiint \nabla(pd\Omega) \ (53)$$

$$\oiint \bar{\bar{\tau}}\,\boldsymbol{n}\,dA \ = \iiint \nabla(\bar{\bar{\tau}}d\Omega) \ (54)$$

Body forces act over the entire volume. The most common body force is the force due to gravitational acceleration:

$$\boldsymbol{F_b} = \iiint p\boldsymbol{g}d\Omega \ (54)$$

The definitions of the surface and body forces into the momentum conservation equation after the statement that the control volume is arbitrary and the integrant can be set equal to zero is:

$$\frac{\partial(p\boldsymbol{V})}{\partial t} + \boldsymbol{V}\cdot\nabla(p\boldsymbol{V}) = -\nabla p + \nabla\bar{\bar{\tau}} + \boldsymbol{F_b} \ (55)$$

This is a vector equation with three Cartesian components associated with the ***x,y, and z*** direction. In three dimensions the viscous stress tensor is a 3x3 matrix. To make the problem well defined the nine extra unknowns are expressed in terms of flow variables, specifically velocity components without the addition of extra equations. This approach was first proposed in the first half of the 19th century by Navier and Stokes and resulted in the fundamental set of governing equations of fluid dynamics called ***Navier-Stokes equations***. The final expression of the viscous stress tensor is:

$$\bar{\bar{\tau}}_{ij} = 2\mu\left[\varepsilon_{ij} - \frac{1}{3}\nabla \cdot \boldsymbol{V}\, \delta_{ij}\right] (56)$$

$$\varepsilon_{ij} = \frac{1}{2}\left[\frac{\partial ui}{\partial xj} + \frac{\partial uj}{\partial xi}\right] (57)$$

Where $\boldsymbol{\varepsilon_{ij}}$ is the strain rate tensor describing the rate of change in the fluid elements, $\boldsymbol{\delta_{ij}}$ is the Kronecker delta and $\boldsymbol{\mu}$ the dynamic viscosity of the fluid.

The final differential equations for the conservation of momentum become:

$$p\left(\frac{\partial \boldsymbol{V}}{\partial t} + \boldsymbol{V} \cdot \nabla\, \boldsymbol{V}\right) = -\nabla p + \mu \nabla^2 \boldsymbol{V} + \frac{\mathbf{1}}{\mathbf{3}}\mu\, \nabla(\nabla \cdot \boldsymbol{V}) + \boldsymbol{F_b}\ (58)$$

Where ∇ is the spatial gradient operator. The form of Eqn. 58 can be expanded into the three dimensions (x, y, z).

5.1.3 Energy equation

The energy equation is the expression of the first law of thermodynamics, and it is summarized in the above statement. The total energy change in the system equals the difference between the heat transferred to the system and the work done by the system on each surrounding. The Lagrangian form is:

$$\frac{dE}{dt} = \dot{Q} - \dot{W}\ \ (59)$$

The total energy as the integral over the fluid volume is:

$$E = \iiint p\left[e(T) + \frac{1}{2}V^2 + gz\right] d\Omega\ \ (60)$$

The first term is the internal energy per unit mass, and it is a function of fluid temperature, the second term is the kinetic energy per unit mass and the third term is the potential energy per unit mass of the fluid.

For conduction heat transfer:

$$q = -k\nabla T\ (61)$$

For the system works:

$$\dot{W}(pressure) = \oiint p(\boldsymbol{V} \cdot \boldsymbol{n})\, dA \ (62)$$

$$\dot{W}(viscous) = \oiint (\bar{\bar{\tau}}\, \boldsymbol{V})\boldsymbol{n}\, dA \ (63)$$

The final expression of the energy equation considering the control volume is arbitrary, hence the sum of all integers must be zero and can be expressed as:

$$\frac{\partial(pe_t)}{\partial t} + \nabla(\boldsymbol{V}(\rho e_t + p) = \nabla(k\nabla T + (\bar{\bar{\tau}} \cdot \boldsymbol{V}) + \dot{S}g \ (64)$$

Where $\dot{S}g$ is a generation source term of energy that refers to the change of total energy that is not expressed by the internal, kinetic, and potential energies.

This chapter describes the governing fluid flow equations. Considering the above equations with the appropriate boundary condition and with the implementation of the correct turbulence model the behavior of the fluid domain both near the body and in the far field can be described.

5.2 Computational Fluid Dynamic: Wing model

5.2.1 Geometry

The wing surface is imported alone at this step without the internal structural parts. The wing has been sectioned and named as leading/trailing edge, wing tip/root, and a hemispherical control volume, which the geometry is shown in Figure 25, is created throughout the wing geometry. The fluid domain is 4 times the dimensions of the wing. The control volume is sectioned and named as far side, near side, outlet, and inlet to specify the boundary conditions at the Fluent Setup. The medium inside the far field is considered air. It is also created a geometry near the wing that is called the body of influence and follows the wing geometry. This type of body will be very useful in the next step (meshing step) and will be analyzed thoroughly below. Once the geometry is created the model is subjected to meshing. The final step is to create two faces of the wing on the leading and trailing edge to refine the meshing in these two areas as there occur the most complicated fluid conditions. The lines that are created are projected to the upper surface of the wing. The whole geometry of the model is presented in Figure 26.

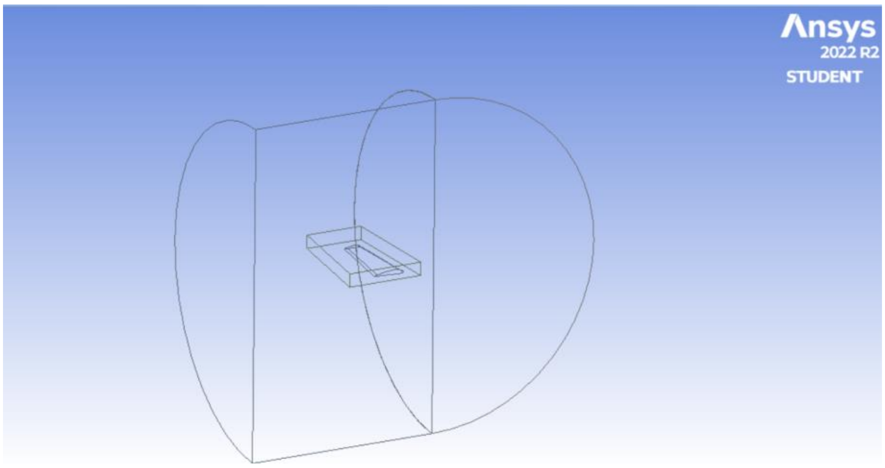

Figure 25. Fluid domain with the control volume and the wing model

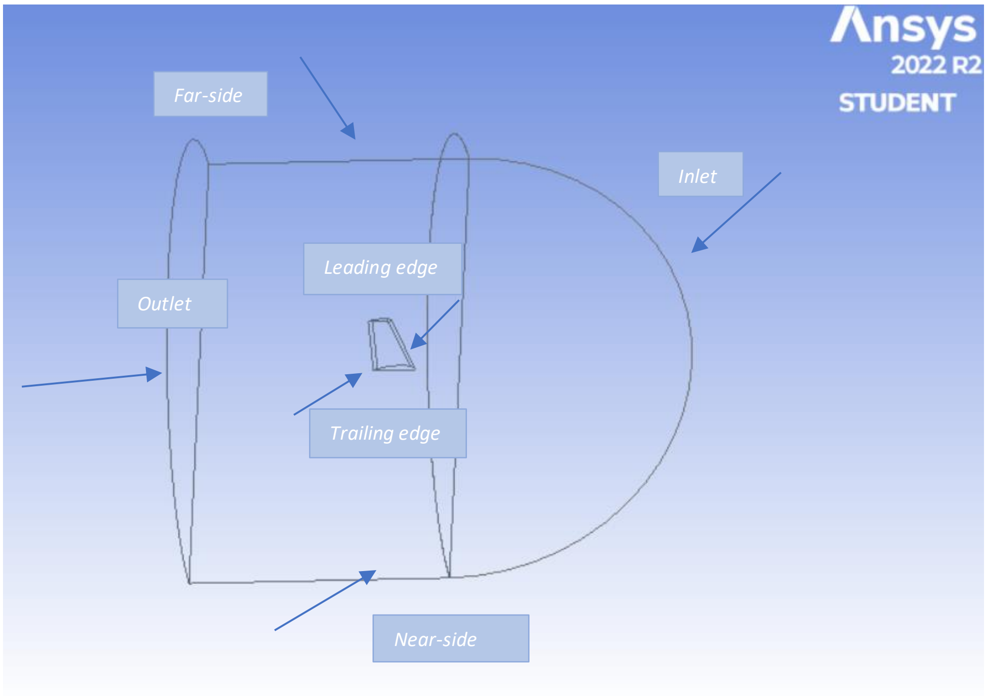

Figure 26. Named and sectioned fluid domain and wing surface

5.2.2 Meshing types

Three-dimensional solid elements for structural analysis include:

- Tetrahedron (Tet), 4 nodes linear interpolation and 10 nodes quadratic interpolation
- Triangular prism (Wedge), 6 nodes linear interpolation, or 15 nodes quadratic interpolation
- Brick (Hex), 8 nodes linear interpolation, or 20 nodes quadratic interpolation

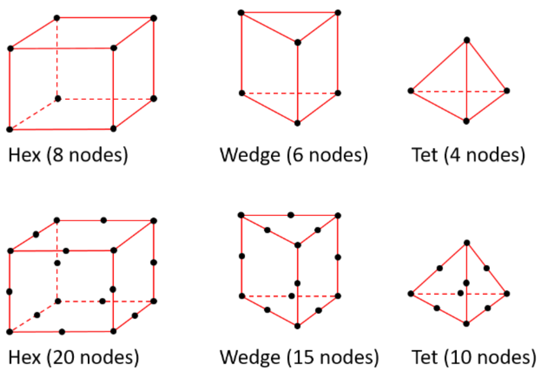

Figure 27. *Three-dimensional solid elements.*

ANSYS FLUENT can use meshes comprised of triangular or quadrilateral cells in 2D bodies and tetrahedral, hexahedral, polyhedral, pyramid, or wedge cells in 3D bodies. The choice of mesh type depends on setup time, computational expense, and numerical diffusion. The theoretical review of mesh types will lead to the right choice of the final body meshing of the experimental 3D wing with the appropriate flow domain [13].

For complex geometries and large-length flow scales, a tetrahedral mesh can be created with far fewer cells than the equivalent mesh with hexahedral elements. Tetrahedral meshing allows the clustering of cells in selected regions of the flow domain. Structured hexahedral meshes will force cells in regions where are not needed. Unstructured hexahedral meshes can offer better quality in moderately complex geometries in contrast to tetrahedral meshes. An advantage of hexahedral elements is that they permit a much larger aspect ratio than tetrahedral cells. A large aspect ratio in tetrahedral cells inevitably affects the skewness of the cell, hence the accuracy of the meshing. Summarizing the above statements for simple geometries hexahedral meshes are preferred, for moderately complex geometries unstructured hexahedral meshes, for relatively complex geometries tetrahedral meshes with prism layers and for extremely complex geometries pure tetrahedral meshes are preferred.

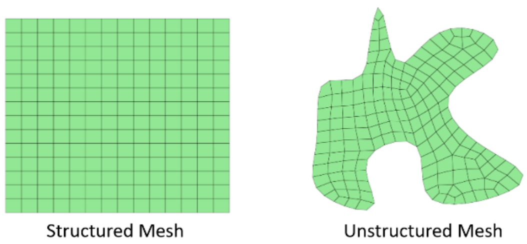

Figure 28. Structured and unstructured mesh

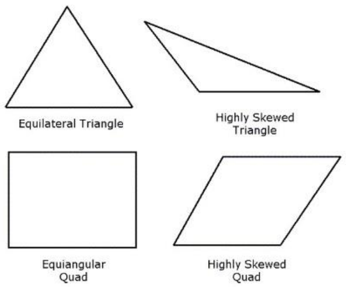

Figure 29. Skewness of cell elements

Meshing controls

Meshing controls enable a more precise mesh. This allows the local meshing to be controlled independently of the global mesh of the whole body. Some examples of local meshing controls include refinement, local sizing, and the sphere of influence.

5.2.3 Meshing the boundary layer

Near-wall models are required for solving the wall-bounded turbulent flow problems. In addition to turbulent models that can be applied, wall functions are used as well to better simulate the fluid behavior in the boundary layers. To analyze these functions, the region near the wall is described in terms of dimensionless variables considering the local wall conditions. The parameter y is defined as the normal distance from the wall while U is the time-averaged velocity parallel to the wall [14]. The dimensionless y+ and u+ can be defined as:

$$u^{+} = \frac{U}{u_{\tau}} \quad (65)$$

$$y^{+} = \frac{y u_{t}}{v} \quad (66)$$

For wall distances $y^{+}< 5$ the layer is dominated by viscous forces. This layer is called the viscous sublayer and it is where the non-slip condition is being produced. The shear stress at this region is assumed to be constant and equivalent to the wall shear stress τ_w. A linear correlation between u+ and y+ leads to : $u^{+} = y^{+}$.

Outside this region turbulence diffusion effects are becoming weaker, and a logarithmic relationship is used to describe the correlation between u+ and y+:

$$u^{+} = \frac{1}{k} ln(E y^{+}) \ (67)$$

This relationship is called log-law and the wall distance $30< y^{+}< 500$ is known as the log-law layer.

The use of the wall functions is to relate the flow variables to the first computational mesh point. The objective at this point is to carefully place the lower limit of y^{+} so that it does not fall into the viscous sublayer. For these reasons, the first CFD cell is calculated below with this formula. The friction velocity u_t are defined as:

$$u_t = \sqrt{\frac{\tau_w}{\rho}} = 0.2622 \ (68)$$

The wall shear stress can be calculated by the skin friction coefficient:

$$\tau_w = \frac{1}{2} C_f p u_{\infty} = 0.0568 \ (69)$$

The skin friction coefficient is calculated from the formula :

$$C_f = 0.058 \ Re^{-0.2} = 0.00389 \ (70)$$

For a value $y^{+} = 30$ the value of y can be calculated as:

$$y = \frac{y^{+} \mu}{u_t \rho} = 1.73 * 10^{-3} m \quad (71)$$

The distance of the first cell from the wall should be 1.73 mm.

5.2.4 Meshing the fluid domain

The model is meshed with an unstructured mesh using the inflation and sphere of influence features in Ansys Workbench. The fluid domain has meshed concerning the body of influence. The advantage of this type of mesh is that it can be adapted to complex geometries. The wing is parametrized concerning the angle of attack (AoA), so the mesh needs to adopt the geometry that occurred every time after the imported angle of attack. Tetrahedral quadratic element meshing is specified on the wing along with its control volume and symmetry. The body of influence has been added to better refine the volume around the wing and it can be controlled how large or how small the refinement is, concerning the size of the body. This means that in the intersection region, ANSYS will use this body of influence to create the desired amount of local mesh refinement, which will influence the flow close to the wing and lead to better simulation results. The meshing is defined by the meshing control of face-sizing of each face of the wing, body sizing concerning the body influence, and inflation. The element size of the face sizing fluctuates regarding the region of the wing. It is used a smaller element size in the trailing and the leading edge of the wing to better calculate the fluid flow in these regions. This will add precision to the solution.

The inflation layer control is designed to create thin elements that can capture the normal gradient with minimal elements. The thickness of inflation layers has been calculated in the previous paragraph.

The number of elements that have been used is 502,943. This is not the optimum number of cells as is shown below by the orthogonal quality factor, but it is a number that is adjusted to the maximum allowable cells that can be used by the Ansys Student license.

Generated mesh is illustrated below:

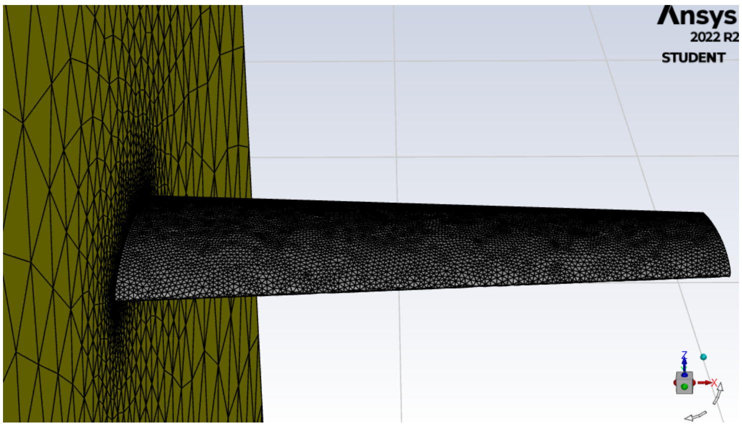

Figure 30. Far side and wing surface meshing.

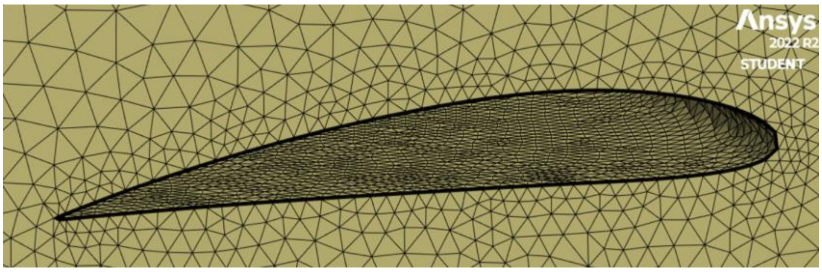

Figure 31. Inflation layers and face sizing of the wing surface.

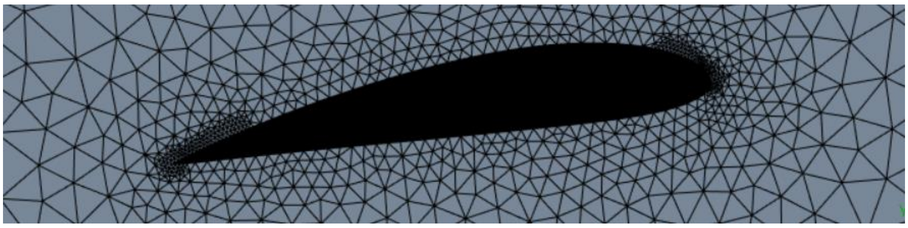

Figure 32. Refinement of the trailing and leading edge.

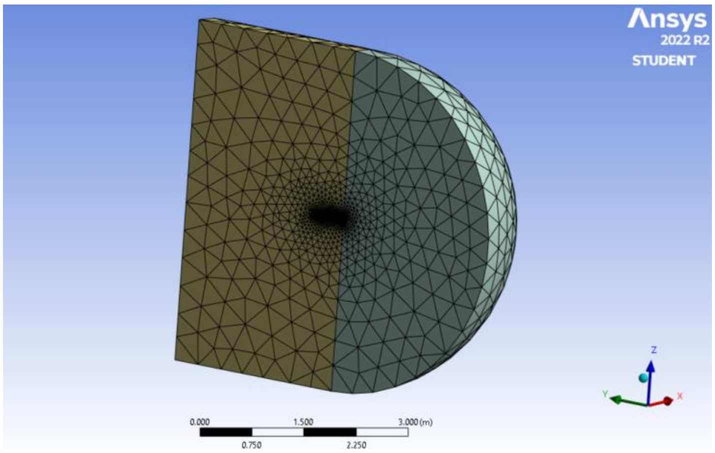

Figure 33. Isometric view of the meshed model.

5.2.5 Meshing quality

The quality of the mesh plays a significant role in the accuracy and stability of the simulation. The attributes that refer to the mesh quality are node point distribution, smoothness, and skewness.

Aspect ratio is a measure of the stretching of cells. It is computed as the maximum value to the minimum distance between the cell centroid and face centroid.

The concept of mesh orthogonality relates to how close the angles between adjacent element faces or adjacent element edges are to some optimal angle, depending on the relevant topology. The orthogonality measure ranges from 0 (bad) to 1 (good). It is shown below in Figure 35, that in the control volume near the wing surface the orthogonal quality is maximum but in the fluid domain far away from the wing the mesh is not refined. This is due to the restriction in the number of cells, but it doesn't affect so much the simulation result as the flow changes near the wing surface and in this way, the simulation is less computationally expensive with small fluctuation of values.

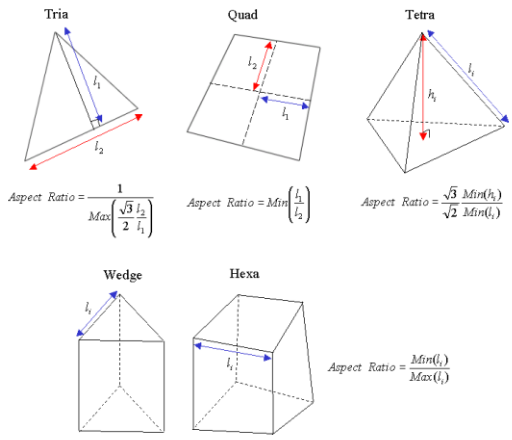

Figure 34. Aspect ratio of 3D elements.

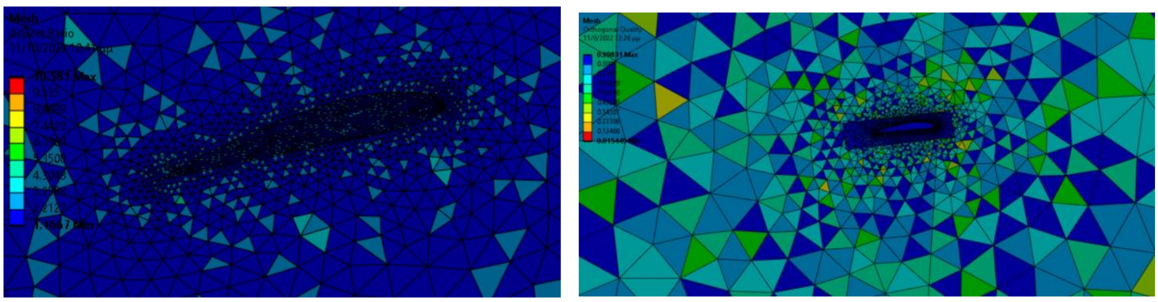

Figure 35. Aspect ratio metrics and Orthogonal quality contours

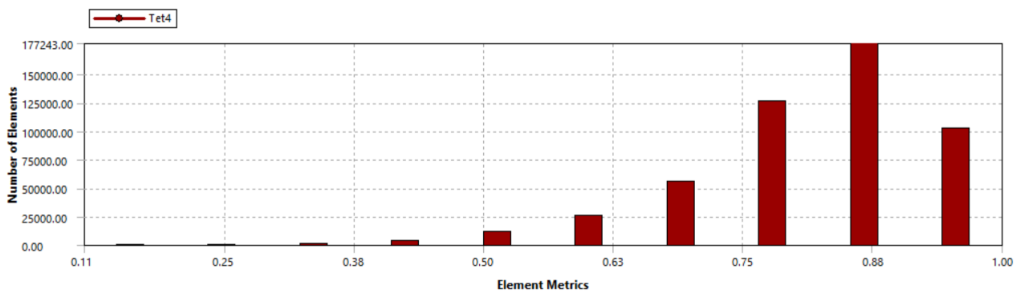

Figure 36. Element metrics of the simulation model

Linear Tetrahedral elements are used through the model and the Nodes are calculated as 93,101 and the elements as 502,943. With Quadradic Tetrahedral elements, the Nodes are calculated as 705,206 and the Elements are the same. Meshing with Quadratic

Tetrahedral elements numerically exceeds the elements allowed by ANSYS student license, so linear Tetrahedral meshing is used.

5.2.6 Choice of Turbulence Model

The choice of turbulence model should depend on the physics of the problem, the required level of accuracy, the available computational power, and the desired simulation time. The correct choice of the Turbulence Model is assumed crucial for the result of the simulation and the available Turbulence Models will be discussed below in detail [15].

Standard k-epsilon turbulence model

This model is based on model equations for the turbulent kinetic energy (k) and its dissipation rate (ε). The model transport equation k is derived from the exact equation, while the model for ε was obtained using physical reasoning. In the derivation of the k-ε, the assumption is that the flow is fully turbulent, and the effects of molecular viscosity are negligible. This model performs poorly for complex flows involving severe pressure gradients and separation. It is preferable for initial studies and iterations for the scope of parametric design.

Shear stress Transport (SST) turbulence model

This model differs from the standard k-ε model concerning the gradual change in the inner region of the boundary layer to a high-Reynolds number version of the k-ε model in the outer part of the boundary layer. Also, the k-ω model includes a modified turbulent viscosity formulation to account for the transport effects of the principal turbulent shear stress. It is suitable for complex boundary layer flows under adverse pressure gradients and separation.

Spalart-Allmaras

The Spalart-Allmaras model is a relatively simple one-equation model that solves a modeled transport equation for the kinematic eddy (turbulent) viscosity. The Spalart-Allmaras model was designed specifically for aerospace applications involving wall-bounded flows and has been shown to give good results for boundary layers subjected to adverse pressure gradients and it is very effective for low Reynolds number flows. It performs purely for flows with strong separation.

Reynolds-Averaged Navier-Stokes (RANS) Equations

RANS Equations are focused on the mean flow and the effect of turbulence on mean flow properties. Before the application of numerical methods, the Navier-Stokes equations were time-averaged. RANS model is suitable for complex 3D flows with strong streamlined curvature. It is tougher to converge considering the close coupling of equations and more CPU time and memory are required in this model.

Appropriate Turbulence model for the model

The flow as it has been thoroughly explained in this chapter is considered a low Reynolds number flow with both laminar and turbulent boundary layers. A ***Standard k-ε*** model is used for this study. ***K-ε*** model in ANSYS FLUENT is the simplest two-equations complete model of turbulence in which the solution of two separate transport equations allows the turbulent velocity and length scale to be independently determined[16]. The turbulence kinetic energy ***k*** and its rate of dissipation ***ε*** are obtained for the following transport equations:

$$\frac{\partial}{\partial t}(pk) + \frac{\partial}{\partial xi}(pkU_i) = \frac{\partial}{\partial xj}\left[\left(\mu + \frac{\mu_t}{\sigma_\kappa}\right)\frac{\partial k}{\partial \chi j}\right] + G_k + G_b - p_\varepsilon - Y_M + S_\kappa \ (72)$$

and

$$\frac{\partial}{\partial t}(p\varepsilon) + \frac{\partial}{\partial xi}(p\varepsilon U_i) = \frac{\partial}{\partial xj}\left[\left(\mu + \frac{\mu_t}{\sigma_\varepsilon}\right)\frac{\partial \varepsilon}{\partial \chi j}\right] + \frac{C_{1\varepsilon}\varepsilon}{\kappa}(G_\kappa + C_{3\varepsilon}G_b) - \frac{C_{2\varepsilon}\rho\varepsilon^2}{\kappa} + S_\varepsilon \ (73)$$

In these equations G_k represents the generation of turbulence kinetic energy due to the mean velocity gradients, G_b is the generation of turbulence kinetic energy due to buoyancy, Y_M represents the contribution of fluctuating dilatation in compressible turbulence to the overall dissipation rate and $C_{1\varepsilon}$, $C_{2\varepsilon}$, $C_{3\varepsilon}$ are constants with standard values. σ_κ and σ_ε are the turbulent Prandtl numbers for k, ε and S_κ, S_ε are user-defined source terms.

The turbulent viscosity μ_t is computed by combining ***k*** and ***ε*** as follows:

$$\mu_t = pC_\mu\left(\frac{\kappa^2}{\varepsilon}\right) \ (74)$$

Where C_μ is a constant. The model constants have default values as presented below:

$C_{1\varepsilon}$=1.44, $C_{2\varepsilon}$=1.92, C_μ=0.09, σ_κ=1.0, σ_ε=1.3.

These values are experimental values from experiments with air and water for fundamental shear flows. They are working fairly well for free shear flows.

5.2.7 Reference values

On the Reference values task page, the reference quantities are referred to the body where the solver computes the desirable normalized flow field variables. In this paper, the lift and drag coefficients are the output variables of the simulation so the reference values of the area, velocity, length, and density of the wing surface are imported as shown in Table 9.

CFD setup	***Value***
Solver	Pressure based
State	Steady-state
Viscous model	k-epsilon
Material	air
Density	1.1685kg/m^3
Mach Number	0.06
Temperature	300K
Enthalpy	0 J/kg K
Pressure	101325 Pa
Reynolds number	1,7278 x 10^6
Reference Area	0.405 m^2
Reference Length	1.15 m

Table 12. *Reference values in Fluent solver*

5.2.8 Boundary conditions

Velocity inlet boundary condition

Velocity inlet boundary conditions are used to define the flow velocity, along with all relevant scalar properties of the flow, at flow inlets. In this case, the pressure is not fixed but will rise to whatever value is necessary to provide the specified velocity distribution. This boundary condition is appropriate for incompressible flows. The velocity inlet should be not placed too close to the wing surface, since this could cause the inflow stagnation properties to become highly non-uniform.

Wall boundary condition

Wall boundary conditions are used to bound solid regions. It is applied to the wing surface. In viscous flows, the non-slip boundary condition is enforced at walls by default. The non-slip boundary condition in viscous flow assumes that the fluid will have zero velocity relative to the boundary. The physical justification of the above statement is summarized as follows. At a fluid-solid interaction, the adhesive forces (forces of attraction between solid and fluid particles) are greater than the cohesive forces (forces between fluid particles). This imbalance leads to the non-slip condition that brings down the fluid velocity to zero near the surface.

Symmetry

Symmetry boundary conditions are used when the physical problem and the expected pattern of flow have mirror symmetry. In this paper, the problem is simplified by considering symmetry in the XY plane. In the CFD analysis, it is used the model of the one wing. The symmetry boundary condition can be summarized as zero normal velocity at the symmetry plane and zero normal gradients of all variables at this plane. These conditions determine a zero flux across the symmetry plane which is required by the definition of symmetry. Since the shear stress is zero it can be interpreted as a slip wall when used in viscous flow calculations.

Pressure outlet boundary condition

The pressure outlet boundary condition requires the specification of gauge pressure at the outlet boundary. The static pressure value is always relative to the operating pressure that is specified.

The problem with the boundary conditions involved is presented in Table 13.

Boundary condition	***Type***	***Value***
Inlet	***Velocity inlet(Magnitude and Direction)***	***22.2m/s x-component: 0 y-component: cos(a) z-component: sin(a)***
Outlet	***Pressure outlet***	***Gauge pressure: 0 Pa Operating pressure:101325 Pa***
Wing surface	***Wall***	***V=0***
Near side	***Symmetry***	***Half wing***
Far side	***Wall***	***V=0***

Table 13. *Boundary conditions of the model.*

5.2.9 Convergence criteria ANSYS

After 156 iterations the lift and drag converged to a final value. The final results and residuals at 0° AoA after the CFD convergence are presented below:

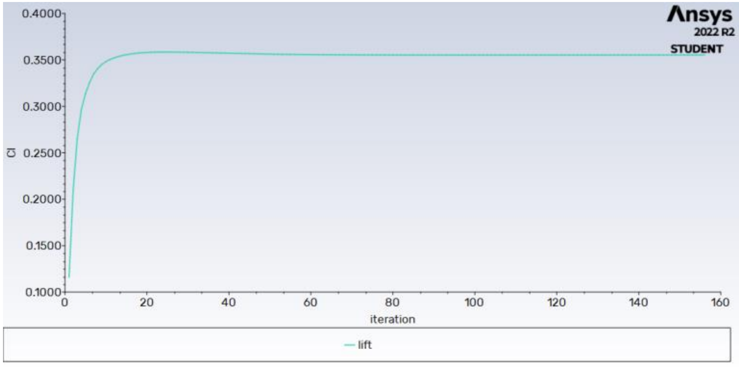

Figure 37. *Lift coefficient convergence.*

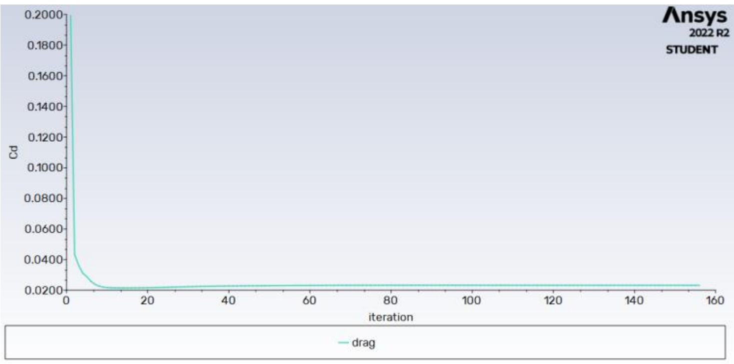

Figure 38. *Drag coefficient convergence.*

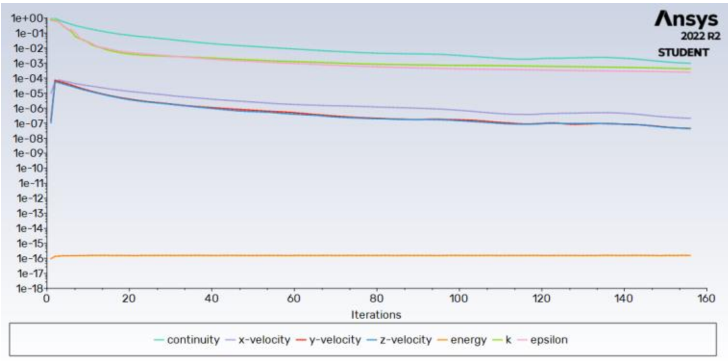

Figure 39. *Scaled Residuals.*

5.3 Simulation Results

5.3.1 Calculation of aerodynamic coefficients

For the postprocessing of the calculation of the external flow field of the wing in the current study, the most notable thing is the lift and drag characteristics of the wing. The problem is converging after 156 iterations. In this set up the main objective is to calculate the aerodynamic coefficient for multiple angles of attack. The problem is parametrized by setting as input parameters the angle of attack of the wing and the angle of the control volume, to ensure better mesh quality. The output parameters are the lift coefficient ***Cl*** and the drag coefficient ***Cd***. The results of each iteration and the final convergence are shown in Figures 37, 38, and 39.

The results for various AoA are presented in Table 14.

AoA	Cl	Cd
0	0.35521671	0.023229133
3	0.59667661	0.034029435
5	0.75840925	0.04425942
8	0.99048128	0.066138992
10	1.132267	0.083659926
12	1.264176	0.10372926

Table 14. *CFD results*

5.3.2 Pressure contours

The contours of pressure obtained for various angles of attacks from the CFD analysis that was presented above are shown in Figures 40 and, 41. The first way to specify that the results are correct is that according to Bernoulli's principle the top surface of the wing experience lower pressure, mostly negative pressure (suctioned pressure), compared to the bottom surface. The wing is effectively pushed upward normal to the incoming flow.

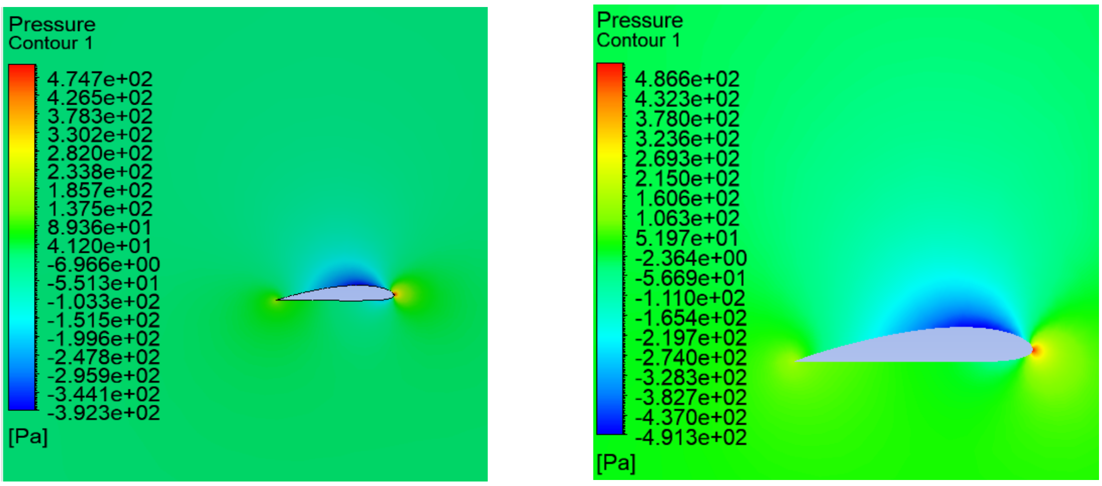

Figure 40. *Pressure contour at 0^o and 3^o AoA*

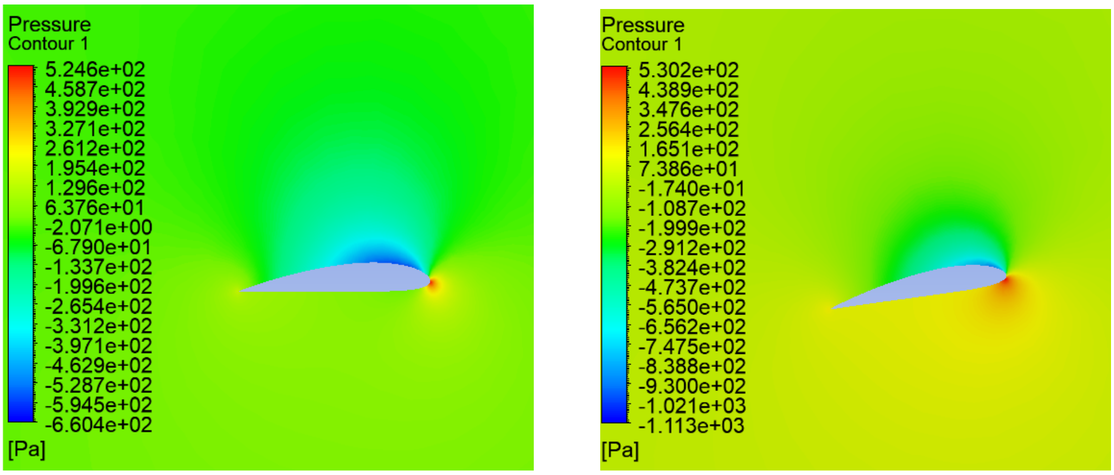

Figure 41. *Pressure contour at 5^o and 10^o AoA*

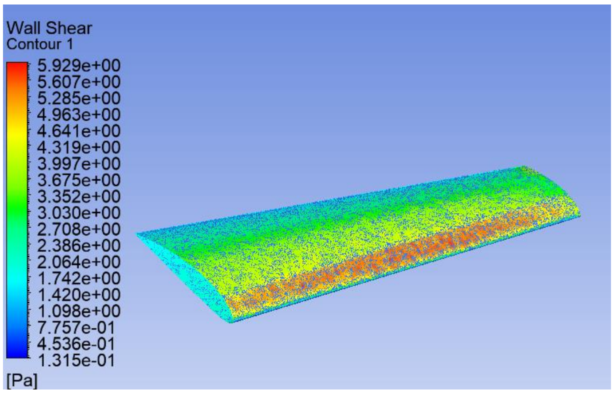

Figure 42. *Shear stress of the wing at 10^o*

The shear stress is maximum at the wing leading edge, which is expected as the velocity is maximum at this area.

5.4 Theoretical Results

The lift curve slope for the finite wing can be determined from the equation below:

$$C_{la} = a_0 * \frac{cos(\Lambda)}{\sqrt{1 + ((a_0 * cos\,\Lambda)/(pi * AR))^2} + a_0 * \frac{cos\,\Lambda}{(pi * AR)}} \quad (75)$$

Where a_0 is the airfoil lift slope.

For a thin airfoil of any shape, the lift slope is estimated at 0.11 per degree. The total lift coefficient is calculated as:

$$C_l = a * C_{la} + C_{l0} \quad (76)$$

Where C_{l0} is the airfoil lift coefficient at zero angle of attack and is obtained from Chapter 3. Under these assumptions, the solution of the Prandtl equation for the General Lift distribution concludes in Eqn. 77 that calculates the induced drag coefficient.

$$C_{di} = \frac{C_l^2}{pi * e * AR} \quad (77)$$

The total drag coefficient can be now expressed as:

$$C_D = C_{D0} + \frac{C_L^2}{\pi * A * e} \quad (78)$$

5.5 Validation of Results

Results from XFLR software with two different solution methods, the Lifting Line Theory method, and the Vortex Lattice Method, are described below with the results of the CFD simulation and the analytical results.

5.5.1 Lifting Line Theory Method (LLT)

This theory is based on Prandtl lifting-line theory, and it applies the concept of circulation and the Kutta-Joukowski theorem. The hypothesis upon which the theory is based is that a lifting wing can be replaced by a lifting line and that the incremental vortices shed along the span trail behind the wing in straight lines in the direction of the freestream velocity. The strength of these trailing vortices is proportional to the rate of change of the lift along the span. The trailing vortices induce a velocity normal to the direction of the free-stream velocity. The effective angle of attack of each section of the wing is therefore different from the geometric angle of attack by the amount of the angle (called the induced angle of attack) whose tangent is the ratio of the value of the induced velocity to the value of the freestream velocity. The effective angle of attack is thus related to the lift distribution through the induced angle of attack. In addition, the effective angle of attack is related to the section lift coefficient according to two-dimensional data for the airfoil sections incorporated into the wing. Both relationships must be simultaneously satisfied in the calculation of the lift distribution of the wing [17].

5.5.2 Vortex Lattice Method (VLM)

A VLM method has been implemented as an alternative, for the analysis of those wing geometries which fall outside the limitations of the LLT. The main differences from the LLT are:

- The calculation of the lift distribution, the induced angles, and the induced drag is inviscid and linear, and it is independent of the wing's speed and the air's viscous characteristics.
- The method applies to any usual wing geometry, including those with sweep, low aspect ratio, or high dihedral, including winglets.

The principle of a VLM is to model the perturbation generated by the wing by a sum of vortices distributed over the wing's planform. The strength of each vortex is calculated to meet the appropriate boundary conditions. The method can be summarized in Eqn. 79 and, Eqn. 80.

The force acting over each panel is calculated as:

$$F = pV \times \Gamma \ (79)$$

Where:

Γ being the vortex strength

P is the fluid density

V is the freestream velocity

The lift coefficient can be defined as

$$C_L = 1/(pV^2S) \sum_{panels} F_{wz} \ (80)$$

Where F_{wz} the force acting over each panel projected to the vertical wing axis.

5.5.3 Distribution of Lift and Drag Coefficients

The results of these methods are illustrated in Figures 43 and 44 :

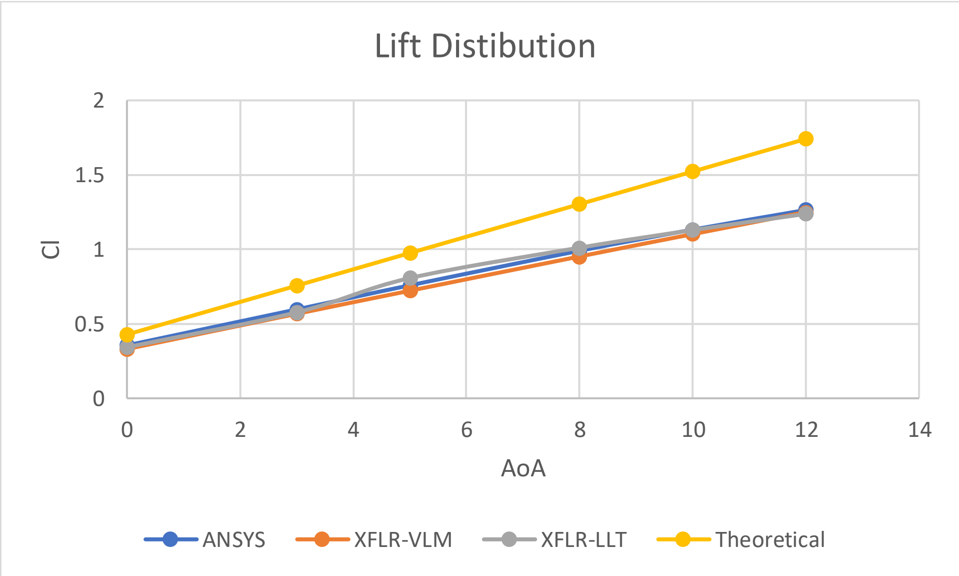

Figure 43. *Lift distribution for various AoA.*

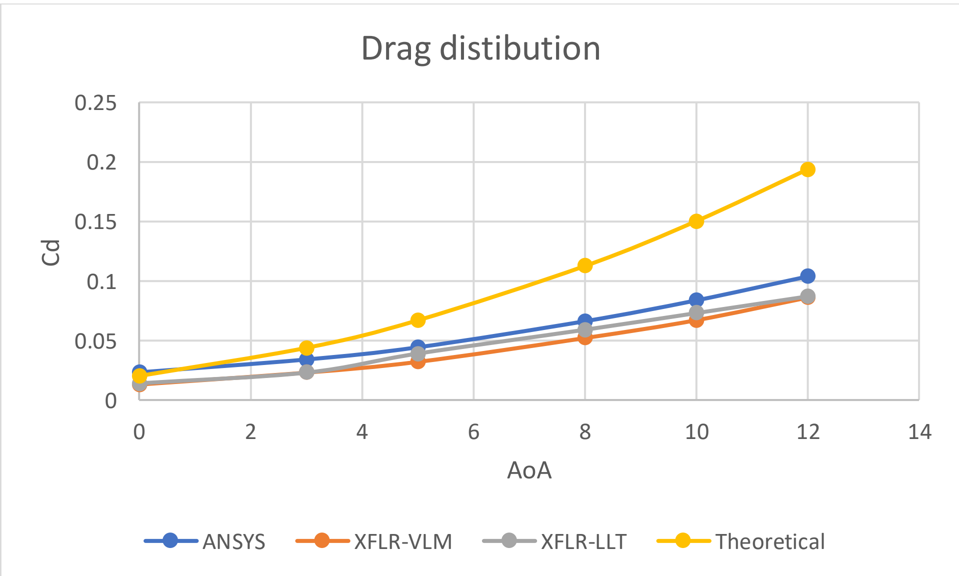

Figure 44*. Drag distribution for various AoA.*

The CFD results from ANSYS FLUENT and the XFLR results are in close agreement. The analytical results show a deviation from the values of the two previous methods as they do not consider the turbulent flow phenomena. The most accurate results are considered to be those obtained from FLUENT as the FEM model that used is much more accurate than the one in XFLR.

6. Structural analysis

Structural analysis can be either linear or non-linear. The linear analysis assumes that the material does not have plastically deformation.

Linear analysis

A linear analysis is an analysis where a linear relation is applied between forces and displacements. This analysis applies to structural problems where stresses remain in the elastic range of the structure's material. In the linear analysis, the stiffness matrix is constant, and the solving process is less computationally expensive than the non-linear analysis, hence a linear static analysis can be used to predict the behavior of the structure before a full non-linear analysis.

In matrix notation, the global system of equations can be expressed as:

$$\boldsymbol{Kv} = \boldsymbol{F} \quad (81)$$

Where $\boldsymbol{K}$ is the system stiffness matrix, $\boldsymbol{v}$ is the vector of unknowns, and $\boldsymbol{F}$is the force vector.

In the linear analysis:

- The model only undergoes small deformations based on the applied forces. Small deformations refer to the linear portion of the stress-strain curve.
- The material does not experience plastic deformation.
- The boundary conditions remain the same throughout the simulation

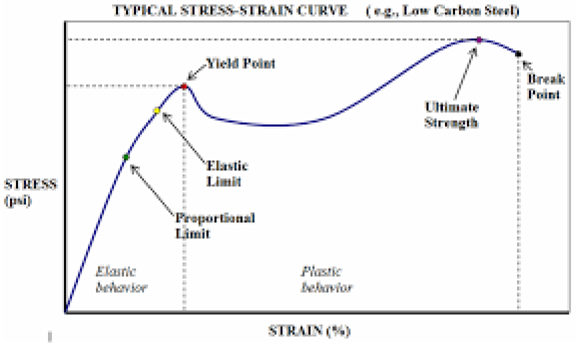

Figure 45. Stress vs. strain curve, highlighting the linear behavior of the material until reaching the yield strength point.

Non-Linear analysis

A non-linear analysis refers to nonlinear relations between applied forces and displacements. Nonlinearity may result from geometrical nonlinearity, material, or contact. The analysis can be characterized by:

- Geometric nonlinearity, where large deflection creates nonlinear behavior in the model.
- Material nonlinearity, where the plasticity of the model affects the solution.
- Nonlinear boundary conditions where the initial boundary scenario changes when the model is deformed

The non-linear analysis provides a more accurate approach to simulation, specifically if the structure is subjected to large deformations. The FEM software in this case uses iterative methods to solve the changing system of equations and the matrix of stiffness is not constant, unlike the linear analysis. Various mathematical methods are used to perform iterations in the non-linear region including the Newton-Raphson method. In matrix notation the non-linear finite element analysis can be:

$$[\boldsymbol{KU}]\ \boldsymbol{\Delta U} = \boldsymbol{F} \quad (82)$$

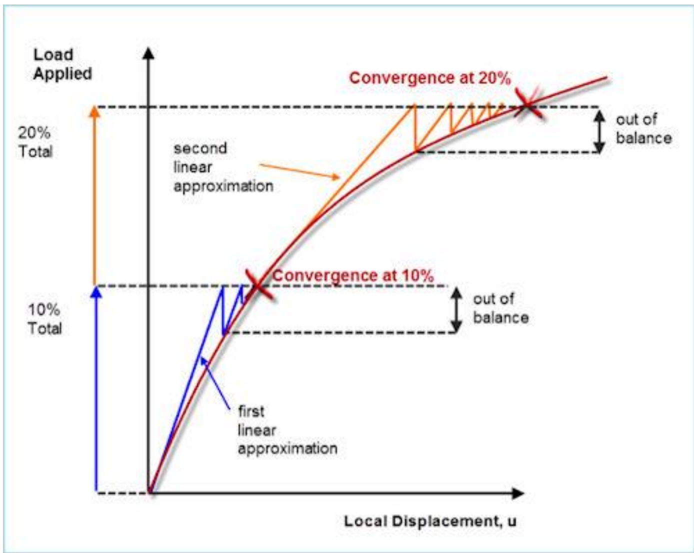

***Figure 46**. Non-linear FEM analysis*

In this study, the experimental wing will be first subjected to linear analysis and if the deformations are very large, indicating non-linear behavior, then it will be subjected to non-linear analysis.

6.1 Aluminum wing

To explore the mechanical effects of the wing subjected to the aerodynamic loads and turbulence during the flight, this chapter presents a finite element analysis of the wing that calculate the deformation, stress, and strain of the wing.

Influenced by the complicated external flight environment, the pressure of the upper and lower wing surface will change with the varying aerodynamic flow field around the wing. Especially, when it applies to the spars, ribs, and skin, the wing will inevitably produce flexure deformation. The scope of this thesis concludes only the investigation of the mechanical effects in the basic structural shape consisting of the two spars, ribs, and skin.

6.1.1 Geometry

The model is redesigned in the *ANSYS Design Modeller* environment. This is very important at this stage as the optimization process requires the parameterization of the thickness of the internal parts of the structure and the position of the spars. This will allow multiple simulations to be performed and form the basis for the structural optimization of the wing. The resulting geometry is shown below in Figure 47.

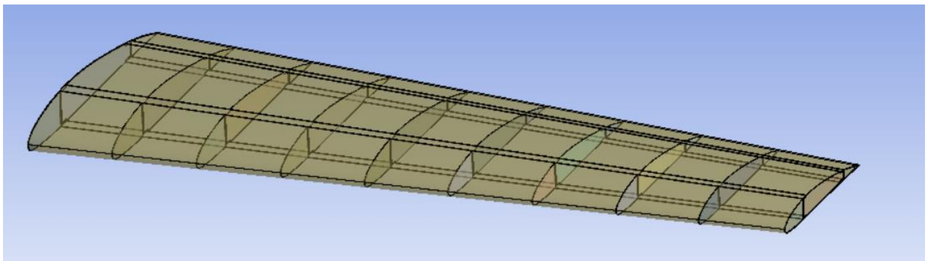

Figure 47. *Inner structure with share topology in Design Modeller.*

6.1.2 Finite element meshing

The wing with the internal structure and skin is then subjected to meshing. Face sizing meshing is used for the skin with 0.01 element size and body sizing with 0.007 element size for the spars and ribs. In the meshing process of the skin, another meshing tool can be used. Virtual topology creates virtual cells and eliminates the edges. The result in the meshing quality is elimination in elements number and refinement.

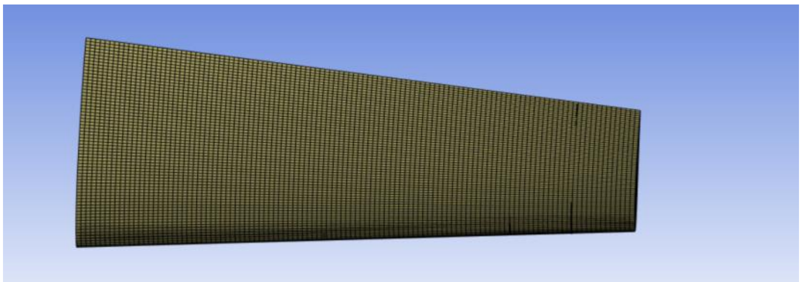

Figure 48. *Face meshing in the skin.*

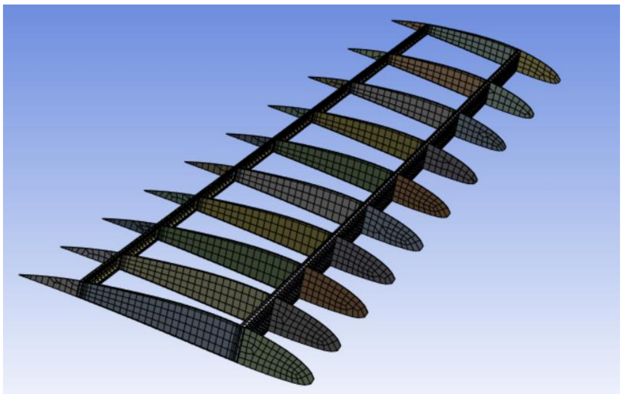

Figure 49*. Face meshing in spars and ribs.*

6.1.3 Boundary conditions

Regarding the global boundary conditions, fixed support is used to represent the physical DOFs of the aircraft wing (three displacements and three rotational), which are fixed on the fuselage of the aircraft and imported pressure load in the skin of the wing to simulate the aerodynamic loads during the flight.

Fixed support

To solve the problem, the boundary conditions must be defined. Fixed support is used to represent the DOFs of the wing which is fixed in the wing root as it is devoted to the fuselage of the aircraft. It is applied both at the root rib and at the edge of the spars that are attached to the fuselage as shown in Figure 50.

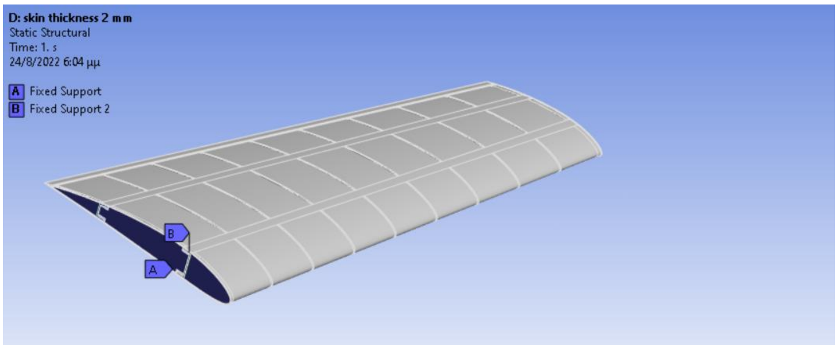

Figure 50. Fixed support in the wing root.

Pressure loads

The second boundary condition is defined as an imported Load (Imported pressure). The fluid flow across the wing surface exerts pressure loads on the structure that cause structural deformation. This type of analysis is called Fluid-Structure Interaction. Fluid-Structure Interaction (FSI) analysis is an example of a Multiphysics problem where the interaction between two different physics phenomena is considered. The importance of the analysis with FSI philosophy is that the performance of the aircraft can be evaluated and analyzed based on the actual aerodynamic distribution of loads in the wingspan instead of using simplified concentrated loads. The analysis based on FSI uses two different solvers to solve the equations for the fluid flow and the structural analysis independently based on numerical solvers. FSI analysis could be a one-way or two-way coupling method, based on the extent of the analysis but the essence is that the information for the solution is shared in both cases.

In one-way FSI analysis the distribution of pressure in the top and bottom skin, calculated in the CFD analysis is transferred to the structure solver to act as a boundary condition in the skin surface of the wing. In two-way FSI analysis, there is another level of coupling, where the displacement of the structure is also transferred to the CFD solver to better calculate the pressure distribution. Using this type of System Coupling, the Fluent and Mechanical simulations can be executed simultaneously with two-way data exchange throughout the simulation. For this study, the one-way FSI has been performed, hence two-way FSI coupling analysis requires large computational power.

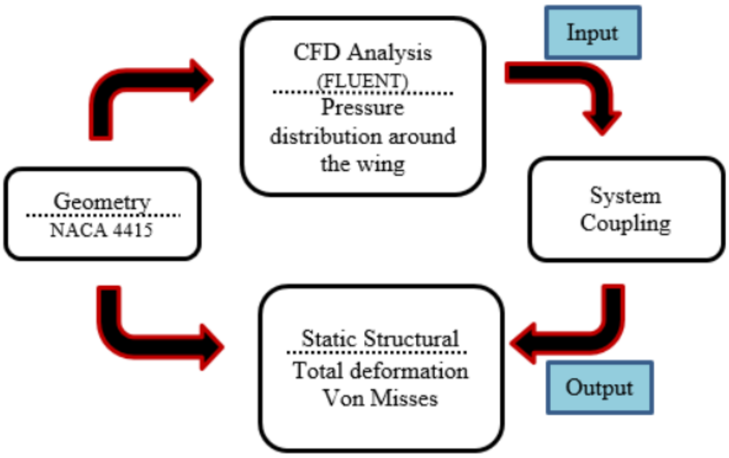

Figure 51. *Flow diagram of one-way FSI analysis*

The imported pressure load from the previous CFD analysis at 10° AoA is shown below to calculate the worst structural scenario. The pressure load also should be scaled by a factor of 2.5 as a load factor of the analysis. The pressure loads that are imported refer to the aerodynamic loads of the **wing surface,** as shown in Figures 52 and 53.

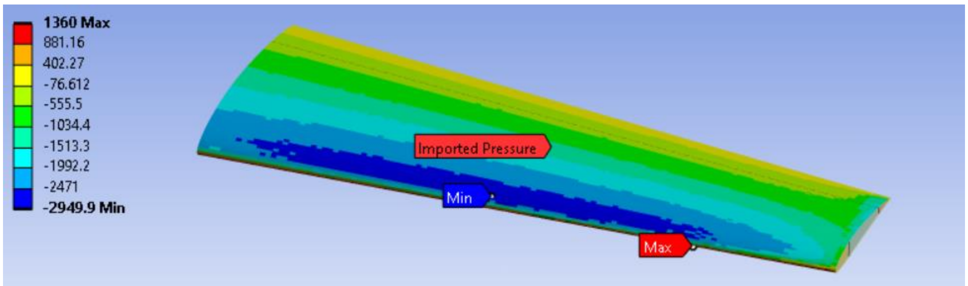

Figure 52. *Imported pressure (Pa) multiplied by a safety factor of 2.5 in the upper skin surface*

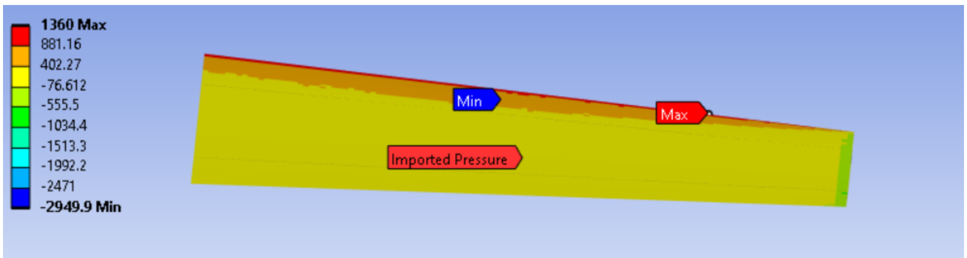

Figure 53. Imported pressure (Pa) multiplied by a safety factor of 2.5 in the bottom skin surface

The pressure is correctly uploaded to the surface of the wing. It can be seen that the upper face of the wing has mostly negative pressure in comparison to the bottom which has positive pressure of a bigger magnitude as it is explained in the previous chapters.

To estimate if the calculated pressure has correctly been imported to the wing geometry the **display source option** can plot every node from the fluid analysis that is transferred in the structural analysis. The pressure distribution is aligned with the wing geometry, Figure 54.

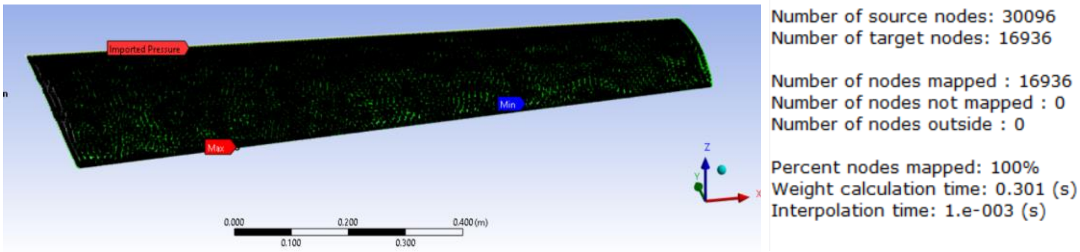

Figure 54. *Display source points of pressure in the wing surface*

6.1.4 Contact regions

In the simulation, the concept of contact and target surfaces are used for each contact region. One side of a contact region is referred to as the contact surface and the other as the target surface. The contact surfaces are restricted from penetrating through the target surfaces. There are different kinds of contact types:

Contact type	***Iterations***	***Separation***	***Sliding***
Bonded	1	No Gaps	No sliding
No separation	1	No Gaps	Sliding Allowed
Frictionless	Multiple	Gaps Allowed	Sliding Allowed
Rough	Multiple	Gaps Allowed	No sliding
Frictional	Multiple	Gaps Allowed	Sliding Allowed

Table 15. Types of Contact Regions

Bonded and No separation types are used in linear analysis and require only 1 iteration. Frictionless, Rough, and Frictional are used in Non-linear analysis and require multiple Iteration. In this study the analysis is linear and the Contact Regions used are Bonded contact regions as Figure 55 presents. Spars and ribs are referred to as contact bodies where the upper and bottom surface of the skin is the target body.

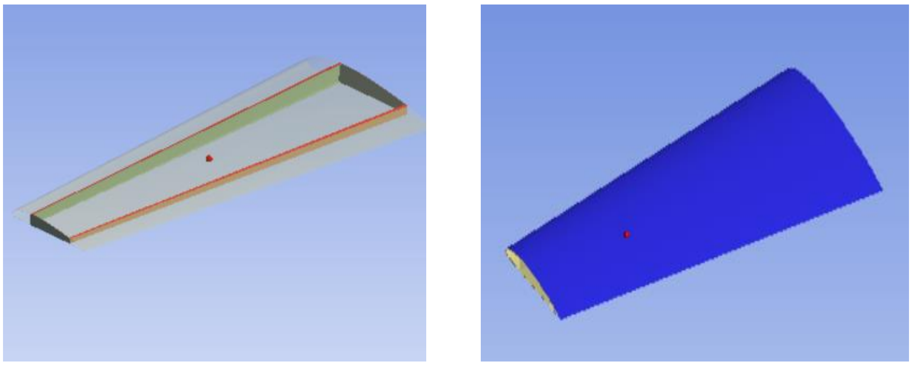

Figure 55. Contact and Target Body of the experimental wing.

6.1.5 Results of Aluminum wing

As elaborated in the methodology, one-way coupling analysis is carried out on the experimental wing to analyze the total deformation and stresses. First, the aluminum wing is examined and then the skin and the two spars are replaced by composite materials. The first model of the experimental wing that will be examined, is an Aluminum 6061 T6 wing. The boundary conditions will be executed as discussed in the above sections. The material properties are demonstrated in Table 16 and the final results are in Figures 56, 57.

Aluminum Alloy 6061 T6	Values
Young's Modulus	69.4 GPa
Poisson's Ratio	0.33
Bulk Modulus	67.686 GPa
Shear Modulus	25.955 GPa
Tensile Ultimate Strength	313 MPa
Tensile Yield Strength	259.2 MPa
Density	2713 kg/m^3

Table 16. Aluminum alloy 6061 T6 structural properties

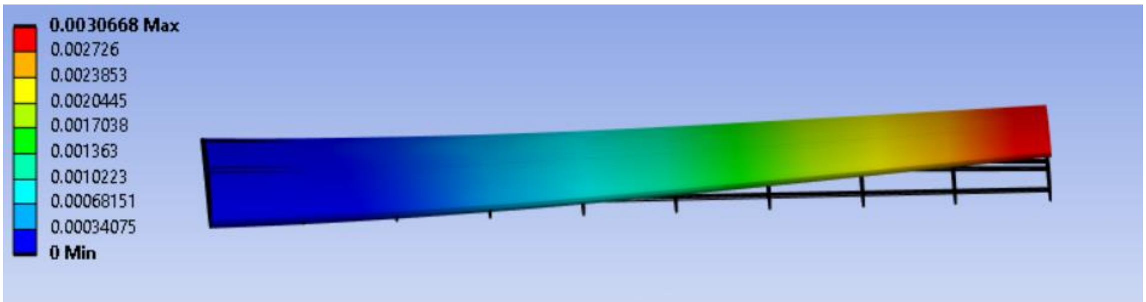

Figure 56. *Total deformation at the initial model*

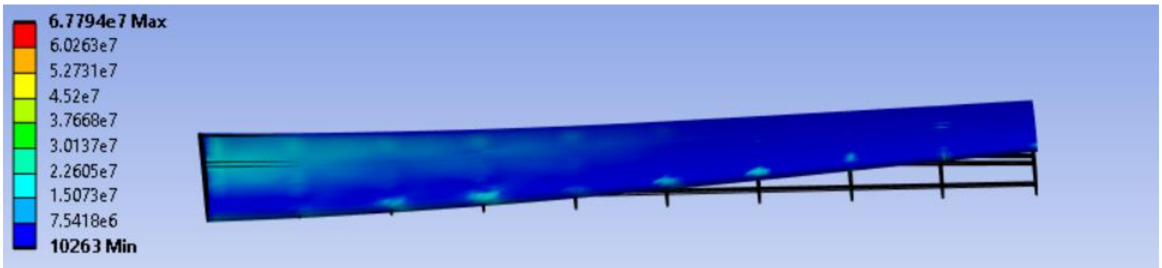

Figure 57. *Equivalent maximum stress (Pa) at the initial model*

The number of ribs is then reduced to 6 due to the overdesigned structure. The simulation results are presented in Figures 58, 59, and Table 17.

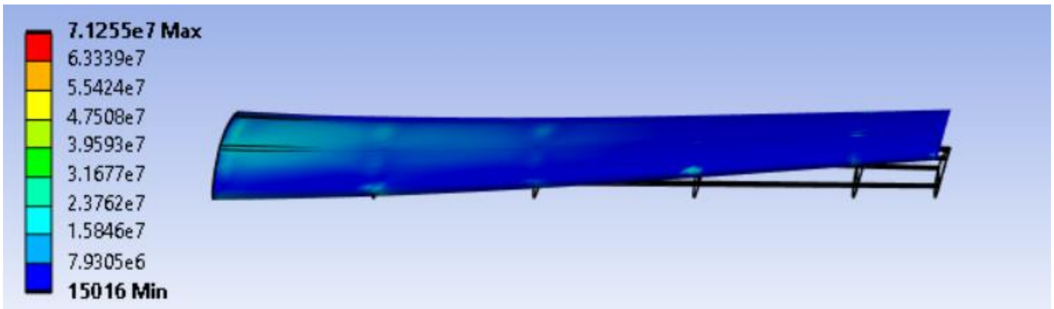

Figure 58. *Equivalent stress (Pa) at the second model.*

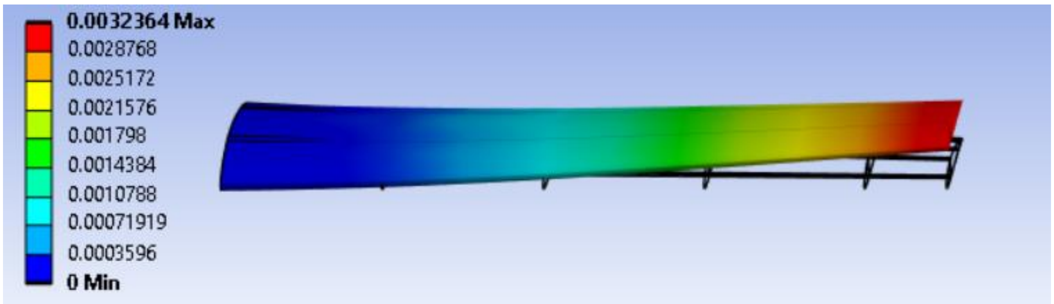

Figure 59. *Total deformation at the second model.*

The maximum equivalent stress and the maximum deformation are slightly increased. Ribs are mainly used to keep the shape of the wing stable while the spars and skin are the main structural elements that prevent the wing from deforming.

Models	*Ribs*	*Total deformation (mm)*	*Maximum equivalent Stress (MPa)*	*Mass (kg)*
Model 1	10	3.0668	67.794	3.4159
Model 2	6	3.2364	71.255	3.2989
Model 3	4	3.3255	72.954	3.2409

Table 17. *Structural Results for the aluminum experimental wing*

The ribs have minimum effect on the mass and the structural properties. The main objective of the ribs in such a small wing is to keep the shape of the skin stable. With the above results, the simulation will continue with 4 ribs.

6.2 Composite wing

The aluminum wing has mass values out of the requirements of this mission. The study will continue with the evaluation and analysis of a composite experimental wing.

6.2.1 Introduction to composite materials

The lightness, strength, and versatility of composite materials make them attractive for multiple applications, especially if the aim is to achieve high-level mechanical performance. All aerospace systems need to be lightweight, hence, to carry more payload, and operate more efficiently. As the operation of UAVs requires heavy payloads, considering the electronics, cameras, and sensors reducing the minimization of the empty weight is vital for their mission. The experimental UAV relies on the power of batteries which shall be 20% of the total weight, so this creates further the need to reduce the weight of the rest of the structure. Today almost all UAV structures are made from carbon fiber composites.

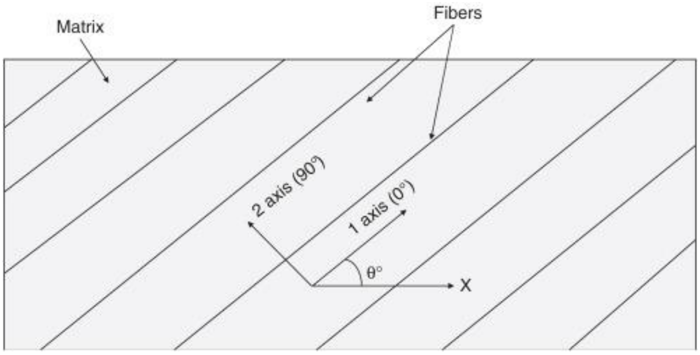

Figure 60. Reference direction of the plies.

Lamina/ply

Figure 60, it is shown the unidirectional fiber-reinforced composite ply also known as the lamina. The coordinate system used to describe the ply is labeled in Figure 60. In this case, axis 1 is defined to be parallel to the 0° fibers (reference direction), the 2-axis is perpendicular and axis 3 is normal to the plane of the plate. This system is the principal coordinate system of the material. If the plate is located parallel to the fibers the modulus of elasticity E11 approaches that of the fibers. If the plate is loaded perpendicular module E_{22} is lower. The material is called anisotropic since the properties are changing with the direction.

Laminate

When the plies, as referred to in the above section, are stacked with various angles the layup is called laminate. Laminas are oriented in directions that will enhance the strength of the structure. Unidirectional laminas are extremely strong and stiff at the 0° direction, but they are much weaker at the 90° direction, and the load must be carried by the polymer matrix. Quasi-isotropic laminates, Figure 61, are made when the orientation of the laminas i is balanced in such a way that the stiffness of the laminate is the same in each in-plane direction[18].

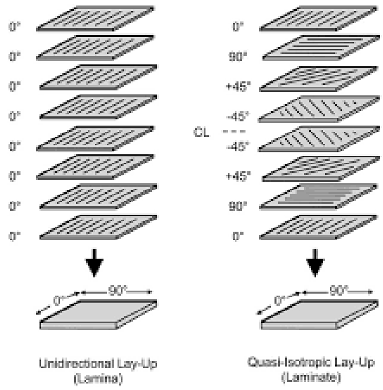

Figure 61. Unidirectional and Quasi-Isotropic Layup.

The scope of this study implies the use of composite materials as the construction weight resulting from the aluminum wing does not meet the requirements of the mission. To properly set up a FEM simulation using composite materials, it is necessary to consider their composite nature, as the direction of laminates can have a significant impact on the mechanical properties of the wing. Ansys Workbench has an integrated tool, Ansys Composite Prep Post (ACP), that allows composite laminates modeling (Pre) and failure analysis of composite materials (Post). In this study, only Ansys composite Prep (ACP) is used, and failure analysis is conducted in the Structural Analysis module with the Tsai-Wu failure criterion.

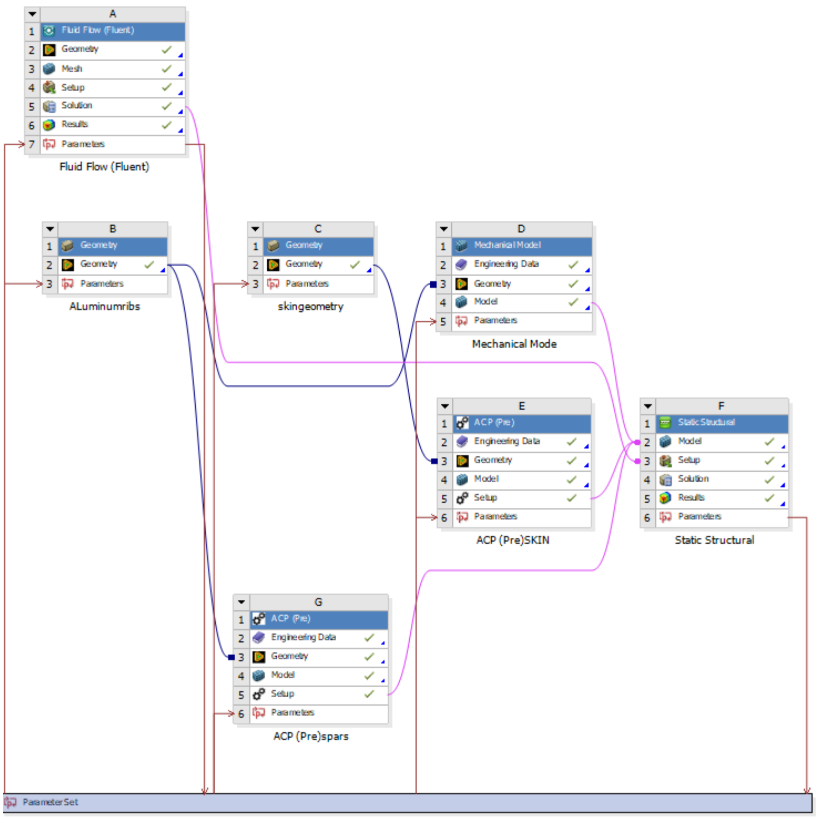

Figure 62. ANSYS Workbench set up for FSI analysis in the composite experimental wing

The ANSYS Workbench setup is demonstrated in Figure 62. The problem is based on a one-way FSI analysis as well. The aerodynamic loads for a 10-degree AoA are imported into the final Static Structural module. The skin and the spars, made of composite materials, are laminated in the ACP tool. The separate parts of the internal structure, composite spars/skin, and the aluminum ribs are then composed in the final Static Structural module with the appropriate *contact regions* and *boundary conditions* and evaluated with the appropriate *failure tools*.

6.2.2 Geometry

The model with the composite materials should be a shell model. The solid parts in the Design Modeller are redesigned to form surfaces with zero thickness. Then the thickness of the surfaces is embedded in the structure in the meshing process.

In the original model, the skin and spars of the wing are transferred to the ACP module and configured with composite materials as shown in Figures 63,64. The layout of the composite with fiber angle orientation and lamina thickness is defined in this section.

6.2.3 Lay-up

The first lay-up that will be used in the skin is $[0/+45/-45/90]_{ns}$. The subscript “s” denotes symmetrical layers, and the notation “n” refers to the number of laminates. This layout is used considering the various loads that the skin can transfer. ±45 plies can carry shear and give buckling stability, 0° plies can carry tension and compression and 90° plies can carry transverse loads and reduce Poisson’s effects. The wing spars must primarily carry shear stresses, and webs made of composite materials should have multiple layers in which each layer has fibers oriented 90 deg or 45 deg relative to fibers in adjacent layers. The stacking sequence that is used in this section is $[\pm45]_{ns.}$ The thickness of each lamina is defined as 0.125 mm.

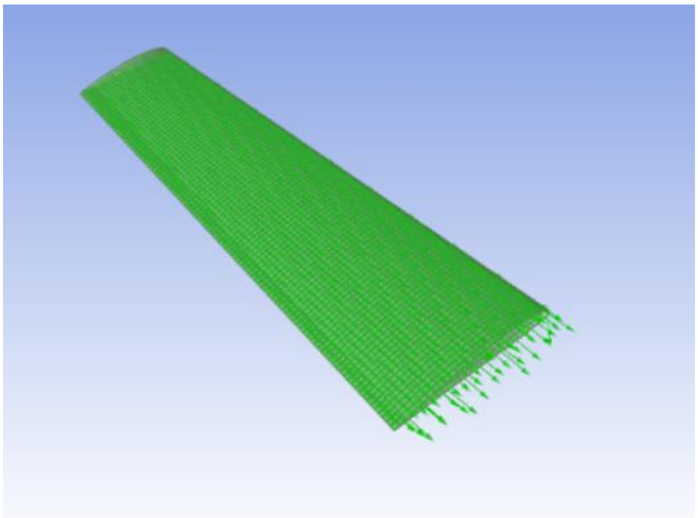

Figure 63. *Lamina 90 degree with fiber orientation at 0 degree*

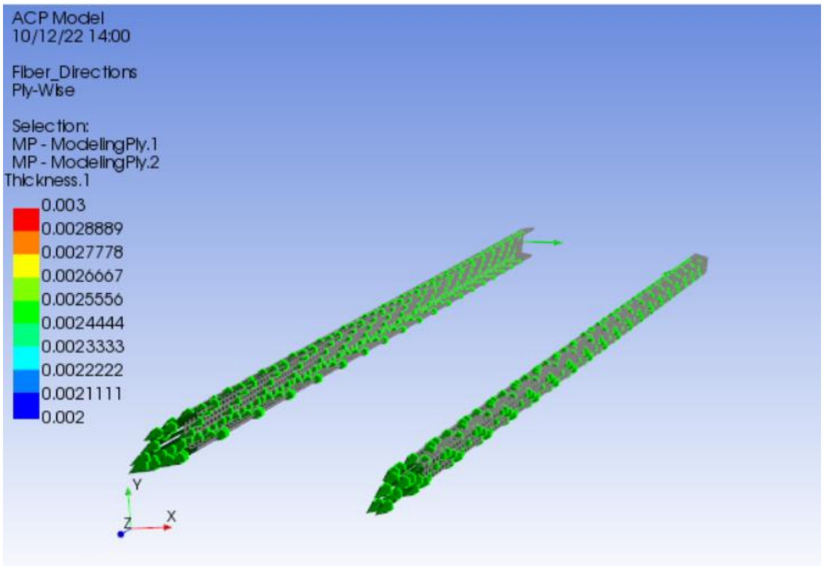

Figure 64*. Laminates on front and rear spar*

6.2.4 Materials

The correct choice of material for composite parts is a combination of both considering the properties of the material and the fabrication method. The most common method used to fabricate aerospace composite parts is using Prepreg. Prepreg is simply a form of the composite where the matrix and the fibers are impregnated together to form rolls as shown in Figure 65. In this experimental wing, Epoxy Carbon Woven Prepreg is the material used for the laminated parts. The material properties are specified in Table 18.

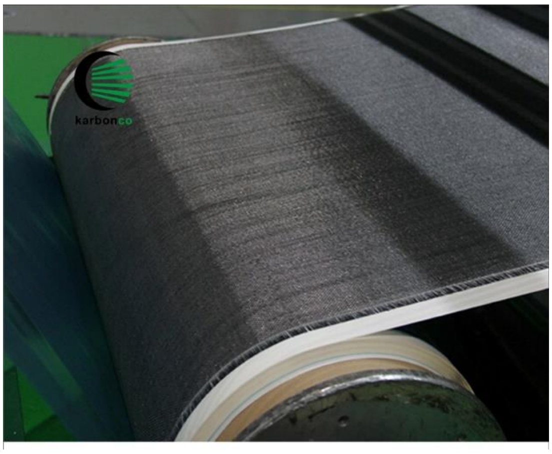

Figure 65*. Prepreg composite*

In this thesis, the XY direction of the reference coordinate system coincides with the main direction of the material. In Table 18, part of the performance properties of materials is defined as follows:

Carbon Epoxy Woven Prepreg	*Value*
Density (p)	*1250 kg/m^3*
E_1 (Young Modulus X direction)	*61.34 GPa*
E_2 (Young Modulus Z direction)	*6.9 GPa*
Poisson's ratio (YZ,XZ)	*0.3*
Tensile X direction	*805 MPa*
Tensile Y direction	*805 MPa*
Compressive X direction	*509 MPa*
Compressive Y direction	*509 MPa*
Shear Modulus XY	*3.3 GPa*
Shear XY	*125 MPa*

Table 18. *Carbon Epoxy Woven Prepreg material properties*

6.2.5 Results

The results for the composite wing for two different laminates are presented in Table 19:

Spars plies	*Skin*	*Spar thickness (mm)*	*Skin thickness (mm)*	*Maximum stress (MPa)*	*Total deformation mm*	*Inverse reverse factor*	*Mass (Kg)*
$[\pm45]_{4s}$	$[0/+45/45/90]_{2s}$	2	1	110	6.1457	0.56923	2.7689
$[\pm45]_{2s}$	$[0/+45/-45/90]_{s}$	1	1	173	10.651	0.88208	1.6957

Table 19. *Results for the composite wing*

There is a reduction in mass of 51.35% regarding the aluminum wing. The contour for the stresses and deformations are presented in Figures 64,65.

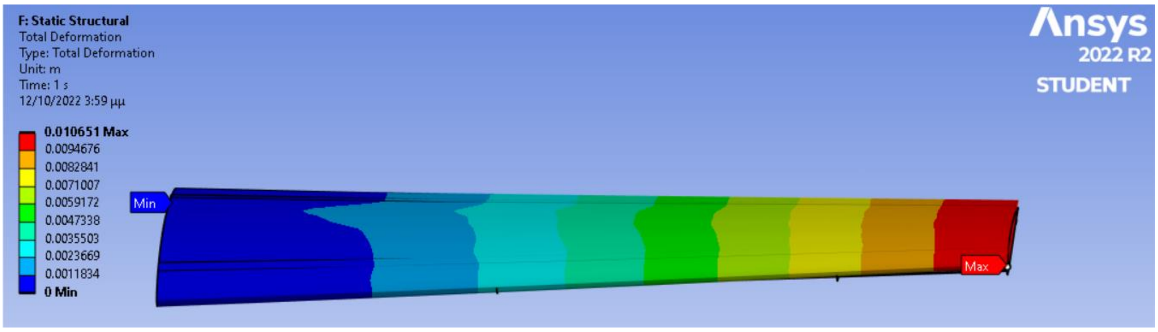

Figure 66. Total deformation in the composite wing (model 2).

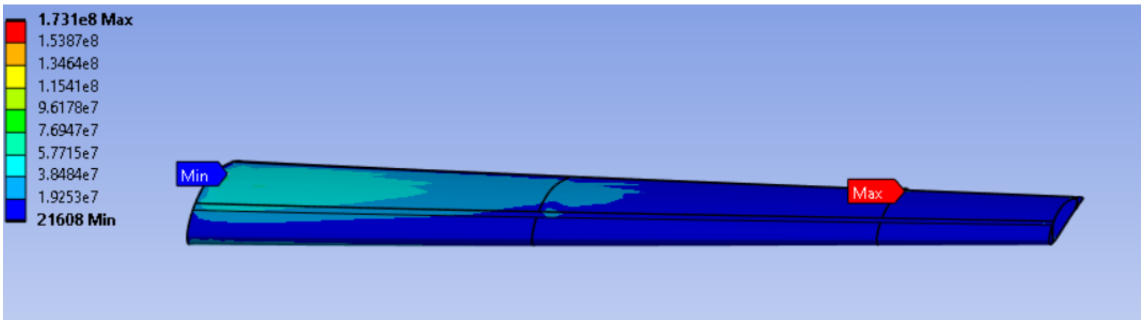

***Figure 67.** Stresses in the composite wing (model 2).*

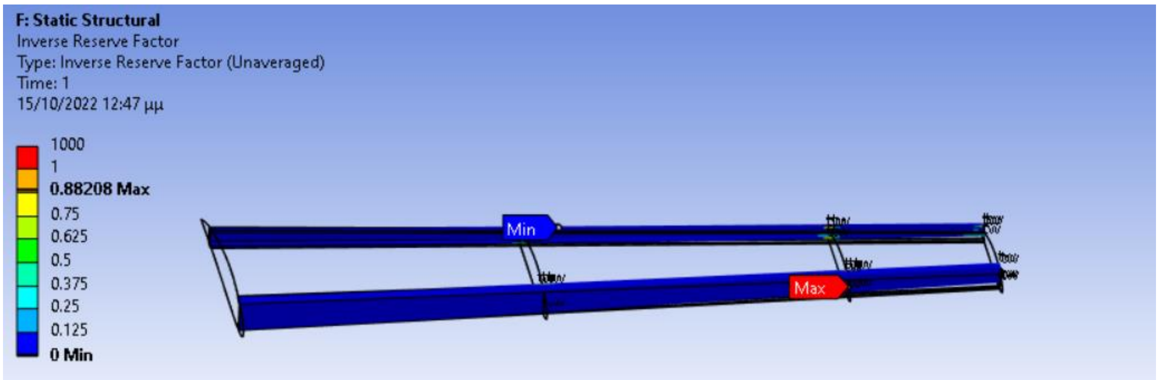

Table 20. Inverse reverse factor failure criterion.

Inverse reverse factor is the parameter used in composite failure. The failure load can be defined as the load value divided by IRF. Hence, when IRF>1 the composite fails, and if IRF<1 it is safe. To avoid unnecessary failure IRF could be maintained between 0.9 and 1.

7. Optimization

7.1 Introduction to optimum design

The design of a system can be formulated as a problem of optimization in which a performance measure of the system is optimized while several constraints and requirements are satisfied. Any problem in which certain parameters need to be determined to satisfy certain constraints can be formulated as an optimization problem. Design, as it has been formulated so far is an iterative process. The essence of this iterative design process is the evaluation of several trial designs until an acceptable solution is achieved. It is always a matter of interest the design starting point based on experience, intuition, and some mathematical analyses. The trial design is then analyzed to determine its feasibility. In the optimization process, one can determine if the solution is the best. The result of this process can take different directions depending on the objectives of the design process [10].

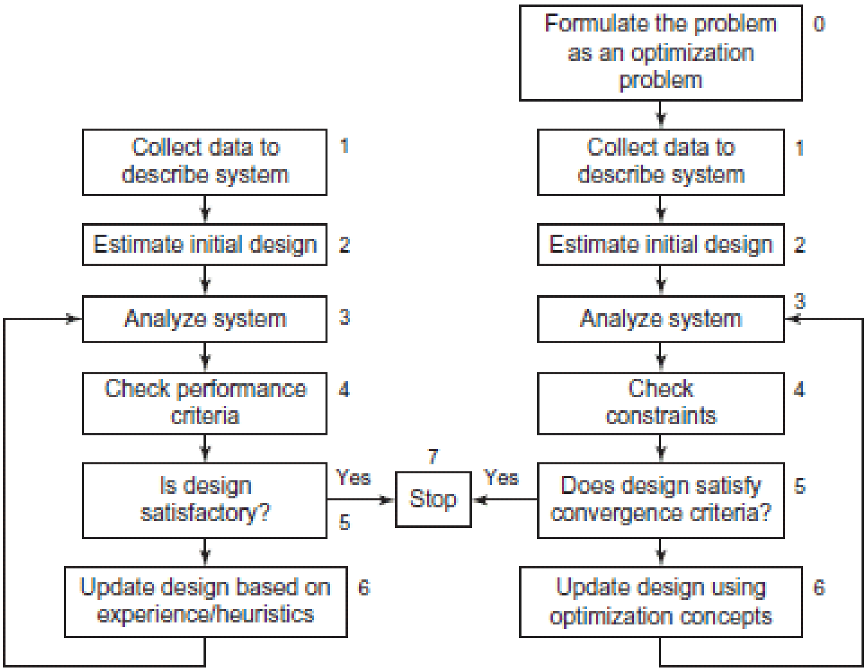

Figure 68*. Block diagram of an optimization design process* [19].

It is generally accepted that a proper formulation of an optimization problem takes roughly 50 percent of the total effort needed to solve it, hence it is vital to follow and adopt well-defined procedures for formulating the design optimization process. The optimal solution can only be achieved by correctly formulating the problem. This can be easily explained as the misplacement of the objectives function or constraints leading to the solution of a different problem from the desired one. Once the correct formulation of the problem is implemented, various software can be found available that can perform the optimization process.

7.2 Optimization model

A general mathematical statement needs to be defined to describe optimization concepts and methods [19]. A minimizing of a cost function while satisfying all the equality and inequality constraints in a specific design space can describe the standard design optimization model that is treated throughout this study. The above statement can be described mathematically as:

$$Find\ a\ n - vector\ x = (x_1, x_2, \dots, x_n)\ of\ design\ variables\ to:$$

$$Minimize\ a\ cost\ function:\ f(x) = f(x_1, x_2, \dots, x_n)$$

$$subject\ to\ the\ p\ equality\ constrains:$$

$$h_j(x) = h_j(x_1, x_2, \dots, x_n) = 0 \quad where\ j = 1\ to\ p$$

$$and\ the\ m\ inequality\ constrains:$$

$$g_i(x) = g_i(x_1, x_2, \dots, x_n) \leq 0\ \ where\ i = 1\ to\ m$$

$$and\ x_i \geq 0\ or\ x_{iL} \leq x_i \leq x_{iu}.$$

The last equation states the upper and lower bound of the design variables where x_{iL} and x_{iu} are the smallest and largest allowed values for x_i , which is included in the inequality constraints. The scope of a general design problem is the minimization of the objective function. However, the maximization of a function *F(x)* is the same as a minimization of a transformed function *f(x)*=-*F(x*). Therefore, the minimization of *f(x)* is equivalent to the maximization of *F(x)*. For the optimization process, one should consider the above statements:

- The functions $f(x)$, $h_j(x)$, $g_i(x)$ are depending, either implicitly or explicitly, on the design variables, otherwise, they have no relation to the optimization problem.
- The number of independent equality constraints must be less than the number of design variables (p ≤ n), otherwise the system is considered overdetermined.
- The number of inequality constraints has no restriction in contrast to the equality ones.

The optimization model is defined in a sphere of all the acceptable solutions. A feasible set for the design problem is a collection of all feasible designs. Mathematically the set S is used to represent the collection of design points that satisfy all constraints:

$$S = \{x|, h_j(x) = 0, j = 1\ to\ p;\ \ g_i(x) \leq 0, i = 0\ to\ m\} \quad (83)$$

The feasible region shrinks when more constraints are added to the problem and the number of possible designs that can optimize the objective function is reduced.

7.3 Optimization method

This thesis aims to formulate an optimization design problem for the experimental wing, that can be efficiently used by an available optimization algorithm. The design process, after conducting several case studies on various trial designs should complete within the optimization environment, to minimize the structure mass, subject to stress and deformation constraints. This implies defining parameters in the construction that are linked to the mass as well as to the structural properties, to formulate a feasible optimization problem. The optimization process is linked to the Finite Elements Results, that have been obtained throughout the processes of the above chapters, and geometry dimensions as the thickness and position of the wing's internal parts (ribs, skin, spars) are directly connected with resulting stresses and deformations, as it is settled up as a parameter in ANSYS Workbench.

The experimental wing that has been designed so far is characterized by quite small values of loads, stresses, and deformations and none of the available structural criteria seems to be violated up to this point of the design process. As minimizing the wing's mass, is the main objective of this study, the structural parameters that appear to have the greatest influence on the final mass, stress, and deformation need to be examined. In this experimental model the thickness of the internal parts, as presented in the Composite wing Section, can have minimum values and satisfy the structural requirements even in the worst-case scenario. Hence, the parameters that need to be reevaluated in the optimization process are the position and dimension of the two spars, which seem to be overdesigned throughout the Preliminary design.

The optimization process, using the MIDACO solver, is implemented using Matlab. MIDACO is a solver for numerical optimization problems that can be applied to continuous (NLP), integer (IP), and mixed integer (MINLP) problems for single or multiobjective optimization. MIDACO implements a derivative-free, evolutionary hybrid algorithm that treats the problem as a black box based on an ant-colony optimization algorithm. A black box optimizer does not require the objective ***f(x)*** and constrained ***g(x)*** functions to be expressed in explicit mathematical form, it requires only the returning numerical values of the objectives and the constraints. The values for the objectives and constraints are calculated considering the coupling with Finite Elements analysis. MIDACO solver is based on an evolutionary algorithm known as Ant Colony Optimization (ACO). This method is a nature-inspired optimization algorithm, where a population shares some information to achieve some goal. In nature, if an ant succeeds in finding a food source, it will return to the nest with a chemical pheromone trail marking its path. This chemical trail will be followed by the other ants, hoping to find food again. The essence of this algorithm is based on this biological behavior with artificial "ants". The first points are randomly selected and then use some parameter like "pheromone" to explore the search domain defined by the optimization problem. Figure 70 illustrates how the mixed integer extended Ant Colony Optimizer samples the decision variable search space with a multi-kernel probability density function (PDF).

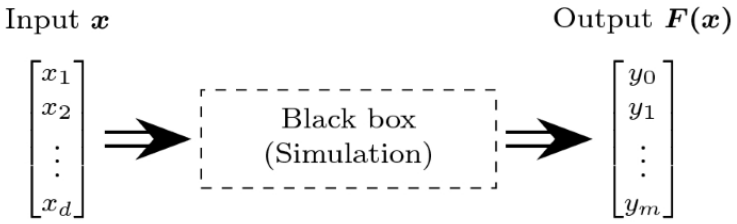

Figure 69*. A black-box optimization method.*

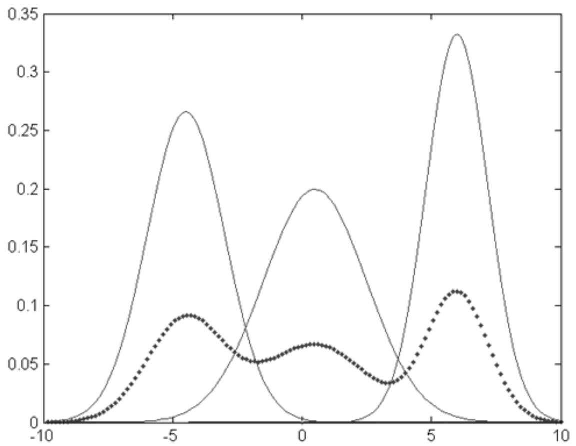

Figure 70*. A multi-kernel PDF based on three individual Gauss PDF's* [20].

7.4 Problem specification

As mentioned in the above section the MIDACO solver is implemented in the problem using Matlab software. It was needed to code and edit some scripts to ensure the interaction with the ANSYS workbench and the MIDACO solver. The code in Matlab is presented in Appendix B. The goal was to find the desirable points that minimize the mass functions. The output parameters from ANSYS Workbench was exported in a csv file after every iteration that performed the optimization algorithm and the desirable output values were obtained. It is possible to formulate the problem in the following way:

$$\min_{x \varepsilon \Omega} F(\chi) = f1(x) \qquad (84)$$

$$subject\ to\ x = [x_1, x_2, x_2, x_4] \quad (85)$$

The optimization variables are listed in Table 21:

x_i	*Value*	*Variable description*
x_1	$0.004 < x_3 < 0.02$ (m)	Length of front spar flanges
x_2	$0.004 < x_4 < 0.02$ (m)	Length of rear spar flanges
x_3	$\{1,2,3,4\}^*$	x position % of the rear spar
x_2	$\{1,2,3,4\}^*$	x position % of the front spar

Table 21. *Optimization design variables.*

In Table 21 the $\{1,2,3,4\}^*$ means 1→35% , 2→30% , 3→25%, 4→10% of wing root chord length for the position of the front spar. For the position of the rear spar, this notation means 1→65%, 2→70%, 3→75%, and 4→80% of wing root chord length.

The constraints for the optimization design problem are specified below:

$$Maximum\ displacement\ < 5\%\ of\ the\ wingspan = 0.05 * 1.15 = 0.0575 \quad (86)$$

$$IRF < 1 \quad (87)$$

Where IRF is the Inverse Reverse Factor of the composite components of the wing. The experimental wing model is subjected to the optimization process with the layers that were presented in the above chapters as it could perform safely with the minimum values of thickness.

The current wing as presented in Chapter 6 has the above structural properties:

Detail	*Value*
Mass	*Total wing:* $1.6957 * 2 = 3.3914$
X position of front spar	25%
X position of rear spar	70%
Front spar flanges	0.02 m
Rear spar flanges	0.02 m
Maximum Total deformation	0.010651 m
Maximum Inverse Reverse Factor	0.8828

Table 22. *Current wing design parameters.*

7.5 Optimization Results

In the optimization process, the MIDACO solver was used for a maximum of 200 iterations considering the power restrictions of the personal equipment. The results obtained are illustrated in Figure 71.

```
OPTIMIZATION FINISHED  --->  MAXEVAL REACHED

        BEST SOLUTION FOUND BY MIDACO
--------------------------------------------
EVAL:       200,  TIME:   18654,  IFLAG:   1
--------------------------------------------
f(X) =                    1.384485462820513
--------------------------------------------
VIOLATION OF G(X)            0.000000000000
--------------------------------------------
g(   1) =     -0.00020916   (IN-EQUAL CONSTR)
--------------------------------------------     BOUNDS-PROFIL
x(   1) =               0.008134835916129;  %  ________________x____
x(   2) =               0.008003018832417;  %  _______________x_____
x(   3) =               3.000000000000000;  %  _____________x_______
x(   4) =               4.000000000000000;  %  ___________________XU
```

Figure 71. *Optimization results in Matlab.*

The obtained values are presented and compared to the current wing geometry in Table 23.

Detail	*Value*
Mass	*Total wing:* $1.384485 * 2 = 2.7689$
X position of front spar	10%
X position of rear spar	75%
Front spar flanges	0.0081348 m
Rear spar flanges	0.0080030 m
Maximum Total deformation	0.017291 m
Maximum Inverse Reverse Factor	0.89
Reduction of Mass	18.35 %

Table 23. *Optimization Results.*

Based on the optimized wing geometry was that the spars were tendentiously located away from the center of the wing (x position) when compared to the geometry used. That location makes the spars smaller, as their height depends on airfoil height, decreasing their moment of inertia and as a consequence decreasing the wing mass. The spar flanges are also specified with smaller dimensions than initially defined, as the Preliminary design was considered overdesigned in contrast with similar models.

8. Conclusions

The parametric design and optimization of a structure to maximize its efficiency is a particularly complex process. The steps must be properly structured so that from a multitude of possible configurations that satisfy the mission requirements the optimal one for the desired situation can be found. In this thesis, the aim was to minimize the weight of the structure. The initial wing configuration evaluated by conventional design methods was found to be overdesigned and thus the structure had to be revised.

The number of ribs was reduced from 10 to 4 and their primary role turned out to be the stability of the skin. The optimum spar location and dimensions were determined using the MIDACO solver optimization algorithm. The position of the spars turned out to be ideal closer to the leading and trailing edge of the wing as there the spars dimensions are as small as possible due to the shape of the airfoil and thus have the smallest inertia values.

Also, the configuration of the wing skin and the front/rear spar with composite materials were investigated. The carbon epoxy woven Pregreq material was tested, and a satisfactory configuration of the laminates was found. The symmetric laminate $[90/0/-45/45]_s$ with a lamina thickness of 0.125 mm was applied to the skin satisfying the composite failure criteria and did not lead to wing failure. In addition, in the spars, the symmetrical structure $[-45/45]_{2s}$ was applied to withstand the shear stresses and loads of the wing and with the thickness of 1mm with 2 symmetrical laminates had satisfactory results on the structural response of the wing. With the above methods the final weight, of the configuration of both wings was found to be 2.768 kg which showed a reduction from the original configuration of up to 59.48%.

9. References

[1] D. P. Raymer, *Aircraft design : a conceptual approach*.

[2] “[Airplane Design] Jan Roskam - Airplane Design Part VI _ Preliminary Calculation of Aerodynamic Thrust and Power Characteristics 6(2004, DARcorporation) - libgen.lc”.

[3] L. W. Traub, “Range and endurance estimates for battery-powered aircraft,” *J Aircr*, vol. 48, no. 2, pp. 703–707, 2011, doi: 10.2514/1.C031027.

[4] “Peukert’s law.”

[5] M. Serdar, lyas Karasu, H. Hakan, and M. Turul, “Low Reynolds Number Flows and Transition,” in *Low Reynolds Number Aerodynamics and Transition*, InTech, 2012. doi: 10.5772/31131.

[6] J. Anderson, “Fundamentals of Aerodynamics.”

[7] “Airfoil Tools,” 2022.

[8] “Introduction to Aeronautics: A Design Perspective Second Edition Purchased from American Institute of Aeronautics and Astronautics.”

[9] T. Megson, “Aircraft Structures for engineering students.”

[10] B. Ramin Sedaghati and M. S. Elsayed, “Multidisciplinary Optimization Standardization Approach for Integration and Configurability MOSAIC Project Task 6 WING-BOX STRUCTURAL DESIGN OPTIMIZATION Report 5 Wing Rib Stress Analysis and Design Optimization Associate Professor Principle Investigator for Task 6,” 2006.

[11] J. D. Anderson, “Governing Equations of Fluid Dynamics.”

[12] “ANSYS INNOVATION COURSES.”

[13] “ANSYS Choosing the appropriate Mesh Type.”

[14] L. Chaoqun and Jiyuan. Tu, “Viscous Sublayer”.

[15] “ANSYS.”

[16] “ANSYS-Standard k-e model.”

[17] “Guidelines for QFLR5 v0.03 XFLR5 Analysis of foils and wings operating at low Reynolds numbers,” 2009.

[18] Z. Hasan, “Composite materials,” in *Tooling for Composite Aerospace Structures*, Elsevier, 2020, pp. 21–48. doi: 10.1016/B978-0-12-819957-2.00002-X.

[19] J. S. Arora, *Introduction to optimum design*. Academic Press, 2011.

[20] M. Schlueter, “Nonlinear mixed integer based Optimization Technique for Space Applications Optimization View project,” 2012. [Online]. Available: https://www.researchgate.net/publication/241677611

10. Index

Appendix A

```
%%1st criterion_stall speed
clc

clear all


vs2=10.2;
vs=12;
vs3=13;

vcruise=22.2;

clmax1=1.2;
clmax2=1.2+0.15*1.2;
clmax3=1.2-0.15*1.2;

vmax=1.2*vcruise;
p0=1.225;
AR=7;
t9=0:0.1:4.5;
pcruise=1.1675;
e=0.8;
cd0=0.009;
wlvs=1/2*p0*(vs^2)*clmax1 +0.*t9 ;%%t=w/s|vs
wlvs3=1/2*p0*(vs3^2)*clmax1 +0.*t9 ;
wlvs2=1/2*p0*(vs2^2)*clmax1 +0.*t9 ;
vs=sqrt(117.5*2/(p0*clmax1))
%% cruise
t=1:0.5:200;%%W/S
np=0.55;
vcruise2=25.5;

q=0.5*pcruise*vcruise^2;
q2=0.5*pcruise*vcruise2^2;

wpcruise=np./((cd0*q./t+t./(pi*q*AR*e))*vcruise);
wpcruise2=np./((cd0*q./t+t./(pi*q*AR*e))*vcruise2);
plot(t,wpcruise)
title('accepted values behind the curve')
%% 2nd criterion_maximum speed at cruising altitude
sigma=0.9538;
npr=0.55;

p=1.1685;% at 500m
clmax=1.2;
k=1/(pi*AR*e);
%cdi= (clmax)^2/(pi*AR*e);
cd0=0.022;

t=1:0.5:200;%%W/S
wpvmax=npr./((0.5*p0*cd0*vmax^3).*(1./t)+((2*k)/(p*sigma*vmax)).*t);


%% maximum ceiling criterion
```

```
npr=0.55;
sigma2=0.86489;
p2=1.0595;
E=11.5;
wpceiling=sigma2./((sqrt((2.*t)/p2)*sqrt(k/3*cd0))*((1/sqrt(3)+sqrt(3))/
2*E*npr));

plot(t,wpceiling)
%%
RC=4;
p=1.168;
sigma=0.95;
wprateclimb=sigma./(RC/np)*(sqrt((2.*t)/p)*sqrt(k/3*cd0))*((1/sqrt(3)+sq
rt(3))/2*E*npr);
plot(t,wprateclimb)
%% TAKE OFF CRITERIA
p=1.13;
vend=11;
clmaxto=1.2;
vthrust=1.38;


wstakeoff=(0.5*p*(vend+vthrust)^2 *clmaxto/1.21)+0.*t9;




%% climb rate
np=0.55;

Vv=4.3;
V=23;

G=Vv/V;
%G=0;
wpclimb=np./((cd0*q./t+t./(pi*q*AR*e)+G)*vcruise);
plot(t,wpclimb)
%% FINAL PLOTS

figure(1)
plot(wlvs,t9,wlvs3,t9,'--',wlvs2,t9,'--',t,wpcruise,t,wpcruise2,'g--
',t,wpvmax,'m',t,wprateclimb,t,wpceiling)

legend('vs=12','vs=13','vs=10.2','vcruise=22.2','vcruise=25','maxspeed',
'climbrate','maxceiling')
grid on

grid minor
xlabel('W/S(Nt/m^2)')
ylabel('W/P(Nt/W)')
ve=sqrt((2/p)*103*sqrt(k/cd0))
%% specify the climb rate curve

v=5:36;

p=1.1685;
AR=6.5;
ws=103;
np=0.7;
a=0.25;
k=1/(pi*AR*e);
```

```
Vv=np/a-p.*v.^3*cd0/(2*ws)-2*k*(ws)./(p.*v);
u=0:3;
x2=22.2+0.*u;

xlabel('cruise speed')
ylabel('climb rate')
plot(v,Vv,x2,u)
grid minor


xlabel('v')
ylabel('rate of climb')
title('Rate of climb curve')
%%
v=2.5;
Vv=np/a-p*v^3*cd0/(2*ws)-2*k*(ws)/(p.*v)
%% specify the drag curve
 CL=0:0.001:1.2;
for v=1:length(CL)

L=CL.^2;
CD=0.01+L./(pi*AR*e);
end
plot(L,CD)
xlabel('Cl^2')
ylabel('Cd')




%% specify the endurance curve

n=1.3;
R=1;
np=0.5;
Cd0=0.009;
S=0.8;
W2=95.207;%newton(1.775kg battery pack)
W1=91.198;%1.366kg
p=1.168;
V=14.8;%voltage


c1=16;%capacity
c2=20;



 x=1:35;%velocity m/sec
 u=0:2;
 W=103.48
 y1=0.58+0.*x;
x2=22.2+0.*u;
for v=1:length(x)

E1(v)=R^(1-n)*(np*V*c1/(0.5*p*x(v)^3*S*Cd0+(2*k*W^2)/(p*x(v)*S)))^n;
E2(v)=R^(1-n)*(np*V*c2/(0.5*p*x(v)^3*S*Cd0+(2*k*W^2)/(p*x(v)*S)))^n;

end
h=figure;
plot(x,E1,x,E2,x,y1,x2,u)
```

```
 grid minor

  datacursormode(h,'on');
 xlabel('cruise speed(m/s)')
 ylabel('Endurance(hrs)')
legend("C=16Ah","C=20Ah","minimum Endurance","minimum speed")
title("Endurance curve for different battery capacity")



E=R^(1-n)*np*V*20/(0.5*p*22.5^3*S*Cd0+(2*k*W^2)/(p*22.2*S))

%% specify the range curve

n=1.3;
R=1;
np=0.7;
Cd0=0.015;
S=0.8;
W1=93.296;%newton(9.52kg)
W2=89.973;%9.181kg
p=1.168;
V=14.8;%voltage


c1=16;%capacity
c2=20;



 x=1:30;%velocity m/sec
 u=0:2;

 y1=0.58+0.*x;
x2=22.2+0.*u;
for v=1:length(x)

R1(v)=R^(1-n)*np*V*c1/((0.5*p*x(v)^2*S*Cd0+(2*k*W1^2)/(p*x(v)*S))/x(v));
R2(v)=R^(1-n)*np*V*c2/((0.5*p*x(v)^3*S*Cd0+(2*k*W2^2)/(p*x(v)*S))/x(v));
end
h=figure;
plot(x,R1,x,R2)
 grid minor

  datacursormode(h,'on');
 xlabel('Range(hrs)')
 ylabel('cruise speed(m/s)')
legend("C=16Ah","C=20Ah","minimum Endurance","minimum speed")
title("Endurance curve for different battery capacity")



E1=R^(1-n)*np*V*20/(0.5*p*x(v)^3*S*Cd0+(2*k*W1^2)/(p*22.2*S))
```

Appendix B

```
key = 'Spyridon_Kilimtzidis_(Univ_of_Patras)_[ACADEMIC-SINGLE-USER]';
 problem.func = @(x) Opt_Fun_v3(x);
%%%%%%%%%%%%%%%%%%%%%%%%%%%%%%%%%%%%%%%%%%%%%%%%%%%%%%%%%%%%%%%%%%%%%%%
%%% Step 1: Problem definition     %%%%%%%%%%%%%%%%%%%%%%%%%%%%%%%%%%%
%%%%%%%%%%%%%%%%%%%%%%%%%%%%%%%%%%%%%%%%%%%%%%%%%%%%%%%%%%%%%%%%%%%%%%%

% STEP 1.A: Problem dimensions
%%%%%%%%%%%%%%%%%%%%%%%%%%%%%
problem.o  = 1; % Number of objectives
problem.n  = 4; % Number of variables (in total)
problem.ni = 2; % Number of integer variables (0 <= nint <= n)
problem.m  = 1; % Number of constraints (in total)
problem.me = 0; % Number of equality constraints (0 <= me <= m)

% STEP 1.B: Lower and upper bounds 'xl' & 'xu'
%%%%%%%%%%%%%%%%%%%%%%%%%%%%%%%%%%%%%%%%%%%%%%
problem.xl =[0.004,0.004,1,1];
problem.xu =[0.02,0.0.02,4,4];

% STEP 1.C: Starting point 'x'
%%%%%%%%%%%%%%%%%%%%%%%%%%%%%
problem.x  = problem.xu; % Here for example: 'x' = lower bounds 'xl'

%%%%%%%%%%%%%%%%%%%%%%%%%%%%%%%%%%%%%%%%%%%%%%%%%%%%%%%%%%%%%%%%%%%%%%%
%%% Step 2: Choose stopping criteria and printing options    %%%%%%%%%%
%%%%%%%%%%%%%%%%%%%%%%%%%%%%%%%%%%%%%%%%%%%%%%%%%%%%%%%%%%%%%%%%%%%%%%%

% STEP 2.A: Stopping criteria
%%%%%%%%%%%%%%%%%%%%%%%%%%%%
option.maxeval  = 200;        % Maximum number of function evaluation 
(e.g. 1000000)
option.maxtime  = 60*60*24; % Maximum time limit in Seconds (e.g. 1 Day 
= 60*60*24)

% STEP 2.B: Printing options
%%%%%%%%%%%%%%%%%%%%%%%%%%%%
option.printeval  = 1;  % Print-Frequency for current best solution 
(e.g. 1000)
option.save2file  = 1;     % Save SCREEN and SOLUTION to TXT-files [ 
0=NO/ 1=YES]

%%%%%%%%%%%%%%%%%%%%%%%%%%%%%%%%%%%%%%%%%%%%%%%%%%%%%%%%%%%%%%%%%%%%%%%
%%% Step 3: Choose MIDACO parameters (FOR ADVANCED USERS)    %%%%%%%%%%
%%%%%%%%%%%%%%%%%%%%%%%%%%%%%%%%%%%%%%%%%%%%%%%%%%%%%%%%%%%%%%%%%%%%%%%

option.param( 1) =  0;  % ACCURACY
option.param( 2) =  0;  % SEED
option.param( 3) =  0;  % FSTOP
option.param( 4) =  0;  % ALGOSTOP
option.param( 5) =  0;  % EVALSTOP
option.param( 6) =  0;  % FOCUS
option.param( 7) =  0;  % ANTS
option.param( 8) =  0;  % KERNEL
option.param( 9) =  0;  % ORACLE
option.param(10) =  0;  % PARETOMAX
option.param(11) =  0;  % EPSILON
option.param(12) =  0;  % BALANCE
option.param(13) =  0;  % CHARACTER

%%%%%%%%%%%%%%%%%%%%%%%%%%%%%%%%%%%%%%%%%%%%%%%%%%%%%%%%%%%%%%%%%%%%%%%
```

```
%%% Step 4: Choose Parallelization Factor   %%%%%%%%%%%%%%%%%%%%%%%%%%%%
%%%%%%%%%%%%%%%%%%%%%%%%%%%%%%%%%%%%%%%%%%%%%%%%%%%%%%%%%%%%%%%%%%%%%%%%

option.parallel = 0;  % Serial: 0 or 1, Parallel: 2,3,4,5,6,7,8...

%%%%%%%%%%%%%%%%%%%%%%%%%%%%%%%%%%%%%%%%%%%%%%%%%%%%%%%%%%%%%%%%%%%%%%%%
%%%   Call MIDACO solver   %%%%%%%%%%%%%%%%%%%%%%%%%%%%%%%%%%%%%%%%%%%%%
%%%%%%%%%%%%%%%%%%%%%%%%%%%%%%%%%%%%%%%%%%%%%%%%%%%%%%%%%%%%%%%%%%%%%%%%
[ solution ] = midaco( problem, option, key);




function [f,g]=Opt_Fun_v3(x)

xtrr=[0.0672,0.0896,0.112,0.1344];
xtr=[0.0672,0.0896,0.112,0.1792];


fid  = fopen('last.wbjn','r');
     filen = fread(fid,'*char')';
     fclose(fid);

     filen = strrep(filen,'rearspar' , num2str(x(1)));
     filen = strrep(filen,'frontspar' , num2str(x(2)));
     filen=strrep(filen,'fposition',num2str(xtr(x(3))));
     filen=strrep(filen,'rposition',num2str(xtrr(x(4))));

    filename = strcat('sparpositionfinal',num2str(1),'.wbjn');
    fid  = fopen(filename,'w');
    fprintf(fid,'%s',filen);
    fclose(fid);

    system(strcat('C:\Users\L340\Desktop\diplwmatiki\"ANSYS Inc"\"ANSYS
Student"\v222\Framework\bin\Win64\RunWB2.exe -B -R
sparpositionfinal',num2str(1),'.wbjn'));
    readata=readtable('last.csv');
    dataclear=cell2mat(readata{7,2});
    out=regexp(dataclear,',','split');
     f=str2double(out(20));
     g1=str2double(out(end));
     g=0.01-g1;

    delete('last.csv');
    delete('sparpositionfinal1.wbjn');
```

[Last page]